

Spectral Energy Distribution Fitting of Active Galactic Nuclei using MAGPHYS

Sooryajith Santhosh

(23848325)

under the supervision of
Prof. Elisabete da Cunha
Dr Andrew J Battisti

This thesis is presented in partial fulfilment of the requirements for the Master
of Physics (Astrophysics)



THE UNIVERSITY OF
WESTERN
AUSTRALIA



International
Centre for
Radio
Astronomy
Research

School of Physics, Mathematics and Computing

The University of Western Australia

10/10/2024

This is to certify that:

1. This thesis comprises an original work.
2. Due acknowledgement has been made to all other materials used in the text.
3. The main body of the thesis is ~ 60 (or ~40 for honours thesis) pages, including tables and figures but exclusive of references and appendices.

I authorise the Head of the Department of Physics to make a copy of this thesis to any person judged to have an acceptable reason for access to the information, i.e., for research, study or instruction.

Student: Sooryajith Kizhakkeparambil Santhosh
ID: 23848325

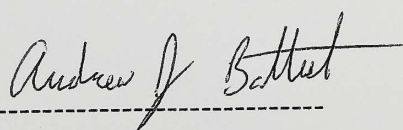
Signature



Date: 18/10/2024

Supervisor: On behalf of Elizabete da Cunha
Andrew J Battisti

Signature



Date: 18/10/2024

Acknowledgements

I acknowledge the Whadjuk Noongar people as the traditional owners of the land on which the University of Western Australia is situated. The Whadjuk Noongar people remain the spiritual and cultural custodians of their land and continue to practise their values, languages, beliefs, and knowledge.

I thank my supervisor Elizabete for guiding and motivating me from the very beginning of this research project. I also thank my co-supervisor Andrew for all the knowledge and ideas shared, and helping me correct the mistakes and for giving valuable feedback on my thesis writing. I also acknowledge the suggestions given during the research group meetings by the senior PhD scholars Juno from UWA and Ravi from Curtin University.

I cannot forget the love and support given by my parents throughout these years. They supported me throughout the Masters program. Love to my brother in India, we grew up together.

Thanks to my friends Sharath, Aakash and Venkitesh for all the motivation and support they gave me throughout the Master's course. They have been a part of my journey for the past 1.5 years.

Lastly, I acknowledge ICRAR for providing the space for working, and UWA for providing the Macintosh machine for my entire research project.

Abstract

A key focus in galaxy evolution research is the study of Active Galactic Nuclei (AGN), which are powered by the accretion of material onto a supermassive black hole, as AGN feedback influences star formation, gas dynamics, and the overall structure of galaxies. They also serve as cosmic beacons, providing insights into the early universe, and help trace the growth of black holes across cosmic time through multi-wavelength observations. We conducted spectral energy distribution (SED) fitting of potential AGN identified in the COSMOS field using infrared color-color selection. The analysis employed a custom version of the **MAGPHYS+AGN** code and was compared with results from **MAGPHYS High-z**. Our results show that the physically derived properties of galaxies can vary significantly when the AGN contribution is excluded from the total infrared emission. We demonstrate that **MAGPHYS+AGN** is effective for modelling galaxies both with and without AGN. Additionally, we improved the AGN version of the code by incorporating physically motivated models for clumpy torus emission, contributing to more accurate SED fitting of AGN-hosting galaxies. The new version of the code constrains the viewing angle and dust density parameters of the AGN torus. However, this new version of the code needs further optimization and testing.

Contents

1	Introduction	1
1.1	Galaxy Spectra and SED fitting	1
1.2	Active Galactic Nuclei	4
1.3	AGN Torus	8
1.4	Research Goal	10
2	Methods & Sample	11
2.1	MAGPHYS	11
2.2	COSMOS2020 catalogue	14
2.3	Sample Selection	15
2.3.1	<i>Spitzer</i> /IRAC selection	15
2.3.2	<i>Spitzer</i> + <i>Herschel</i> color cut	16
2.3.3	Radio loud sources	18
2.4	Control sample	20
2.5	SED fitting	21
3	Results	23
3.1	MAGPHYS highz vs MAGPHYS highz+AGN emp	23
3.1.1	χ^2 comparison	26
3.1.2	Band-wise residual	26
3.1.3	ξ_{AGN} distribution	27
3.1.4	Template selection	31
3.2	Parameter Comparison	31
3.2.1	AGN sample	32
3.2.2	Control Sample	35
3.3	Limitations of AGN emp	35
4	AGN Torus Model	38
4.1	Addition of Torus templates	40
4.2	Testing AGN torus on a robust AGN sample	42
4.3	Summary	44

5 Discussion and Conclusion	45
5.1 Discussion and Conclusion	45
5.2 Summary	47
Bibliography	49
A Student Achievement	54
B Proposal	55
B.1 Introduction	55
B.1.1 Galaxy SED modelling	55
B.1.2 MAGPHYS	57
B.1.3 Active Galactic Nuclei	59
B.1.4 MAGPHYS + AGN model	61
B.2 Research Plan	64

Chapter 1

Introduction

1.1 Galaxy Spectra and SED fitting

Galaxies emit spectra at different wavelengths in varying magnitudes that arise from various physical processes such as emission from stars, dust, gas, etc. The emitted radiation is observed using telescopes that can capture the radiation at specific wavelength ranges. A few examples are X-ray telescopes such as *Chandra X-ray Observatory*, *XMM-Newton*, ultraviolet telescopes such as *Galaxy Evolution Explorer* (GALEX), optical telescopes such as *Hubble Space Telescope* (HST), Very Large Telescope (VLT), infrared telescopes such as *Spitzer Space Telescope*, *Infrared Space Observatory*, *James Webb Space Telescope* (JWST), and radio telescopes like Murriyang (Parkes).

The Spectral energy distribution (SED) of a galaxy shows its energy output as a function of wavelength or frequency across the entire or a specific range of the electromagnetic (EM) spectrum (see Figure 1.1), from which its emission characteristics can be interpreted since the physical processes that happen in a galaxy are imprinted on it's an integrated spectrum. Multi-wavelength SED fitting is the method that compares modelled SEDs with observed data to derive the physical properties of galaxies (Walcher et al., 2010; Conroy, 2013). The various sources of radiation from a galaxy include the ultra-violet (UV) and optical emission from young stars, near-infrared emission from older stellar populations, radiation absorbed and re-processed by the hot gas surrounding young stars or the nebular emission, infrared (IR) radiation from dust heated by stellar emission, radiation from accreting material around a black hole or an active galactic nucleus, or dust heated by the active galactic nucleus. Hence the SEDs of galaxies are shaped by various physical properties that take place within them, such as the formation and evolution of stars over time and space, metal content in the the galaxy, distribution and relative proportions of chemical elements present in the stars, gas, and other components of the galaxy. Hence the dust properties such as dust mass, grain size distribution of the dust in the interstellar medium, star-dust geometry, and interstellar radiation field (pervasive radiation present in the space between stars within a galaxy) can also be analyzed from an observed SED. Examples of commonly derived physical properties are properties of stellar populations such as star formation (SF) history (SFH), stellar metallicity and chemical abundance patterns, total

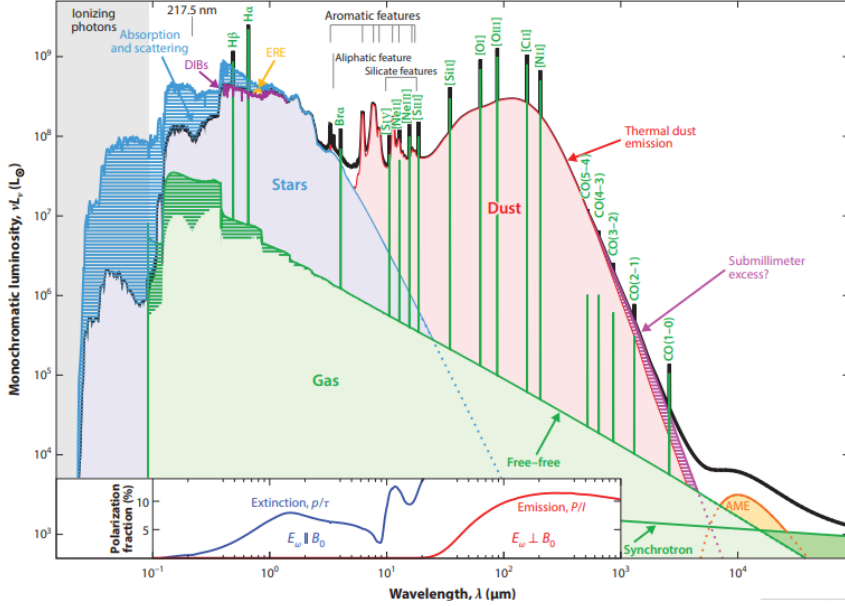


Figure 1.1: SED of a typical star-forming galaxy. The hatched blue indicated stellar emission that is removed due to the dust absorption which is re-emitted in the IR (red) through energy conservation. Stars dominate emission in UV to near-IR wavelengths and dust dominates in the IR. Gas is sub-dominant at UV to IR wavelengths, and can instead be traced through emission features. Figure 1 reproduced from [Galliano et al. \(2018\)](#)

mass in stars, and the physical state and quantity of dust and gas ([Conroy, 2013](#)).

The stellar emission is modelled using stellar population synthesis (SPS) methods, which involves modelling single stellar populations (SSP) that describe the evolution in time of the SED of a single, coevolving stellar population of the same metallicity and abundance pattern, and modelling complex stellar population (CSP) which involves several SSPs. Creating an SSP requires stellar evolution theory in the form of isochrones that describes the population of stars of the same age and metallicity in the Hertzsprung - Russell diagram, stellar spectral libraries spanning a range of effective temperature (T_{eff}), bolometric luminosity (L_{bol}) and metallicity, and initial mass function (IMF) describing the distribution of stars for varying mass.

SED modelling of dust emission is equally important as stellar emission modelling because dust absorbs and scatters UV and optical radiation and re-emits it in the IR wavelength. Since dust acts as an obscurer of UV while emitting in the IR at the same time, the attenuation in UV and emission in the IR are modelled simultaneously in most SED models such as MAGPHYS ([da Cunha et al., 2008](#)) assuming energy balance. Dust attenuation is a consequence of the optical properties of the grains, the grain size and shape distribution, and the relative geometry between stars and dust ([Salim & Narayanan, 2020](#)). It is calculated by comparing the observed vs expected SED from a line of sight. The Calzetti dust attenuation curve ([Calzetti et al., 2000](#)), the MW, LMC, and SMC extinction curves, or the time-dependent attenuation model from [Charlot & Fall \(2000\)](#) are the popular dust attenuation curves used.

Dust grains primarily consist of carbonaceous and silicate compositions ([Draine, 2003](#)). The carbon grains are primarily carbon-hydrogen ring-like molecules or polycyclic aromatic

hydrocarbons (PAHs) for small grain size and graphite for large grain size. The dust emission in far-IR is modelled usually as black body curves from dust of varying temperatures or different physical properties, by considering that the energy absorbed by the dust in the UV is emitted in IR. However, the mid-IR is dominated by stochastically heated (hot) small dust grains and PAHs, which is not well-described by blackbody curves and so is typically modelled using empirically-derived templates (i.e., using mid-IR spectral measurements of galaxies. e.g., [da Cunha et al. \(2008\)](#)).

In the multi-wavelength SED fitting technique, the stellar models are combined with dust emission and attenuation models, then compared with observed data to derive physical parameters such as attenuation and SFH parameters using grid-based χ^2 minimization or Markov Chain Monte-Carlo techniques. There are many SED fitting tools developed over time. Some of the examples are MAGPHYS ([da Cunha et al., 2008](#)), CIGALE ([Noll, S. et al., 2009](#)), BEAGLE ([Chevallard & Charlot, 2016](#)), Prospector ([Leja et al., 2017](#)), ProSpect ([Robotham et al., 2020](#)). Some of these SED fitting codes are becoming increasingly complex, with more free parameters and templates being introduced to capture the diverse physical processes in galaxies. However, this added complexity is not always beneficial. A larger number of parameters increases computational time and many of the parameters may remain unconstrained, making the results highly dependent on the assumed priors for the fitted parameters.

MAGPHYS is an SED fitting code that derives physical properties of galaxies by modeling their stellar and dust emission across rest-frame UV to far-IR using energy balance technique. However, the default version of MAGPHYS SED fitting code (more details of the code will be discussed in Chapter 2) does not consider the effect of another component that can heat the dust and cause IR emission: matter accreting to a supermassive black hole at the centre of a galaxy that heats the dust to produce IR emission in a galaxy.

Supermassive Black Holes (SMBHs) are now recognized as a common feature in the central regions of nearly all local galaxies, influencing their host galaxies through processes like gravitational interactions, accretion, and energy feedback ([Kormendy & Ho, 2013](#)). They grow by either mergers with other black holes ([Volonteri et al., 2003](#)) or by accretion of gas, dust, and other material from their surrounding environment ([Alexander & Hickox, 2012](#)). When actively growing, they release enormous amounts of energy, which is emitted as electromagnetic radiation across multiple wavelengths, ranging from radio to X-rays. These energetic events are crucial for understanding the physical processes occurring near black holes and have significant effects on their host galaxies. Those galaxies in which this kind of nuclear emission happens by the accretion onto a central black hole are called active galactic nuclei, and the radiation emitted by the central accretion or the emission from dust heated by the AGN is called the AGN component. The derived galaxy parameters and the galaxy SED fitting can be affected if the galaxy has an AGN component along with the stellar emission component. In SED fitting, it is essential to model AGN emission alongside stellar emission and dust emission heated by star formation, as AGNs contribute significantly to the total energy output of certain galaxies. However, AGN emission presents unique challenges since it cannot be accurately captured using

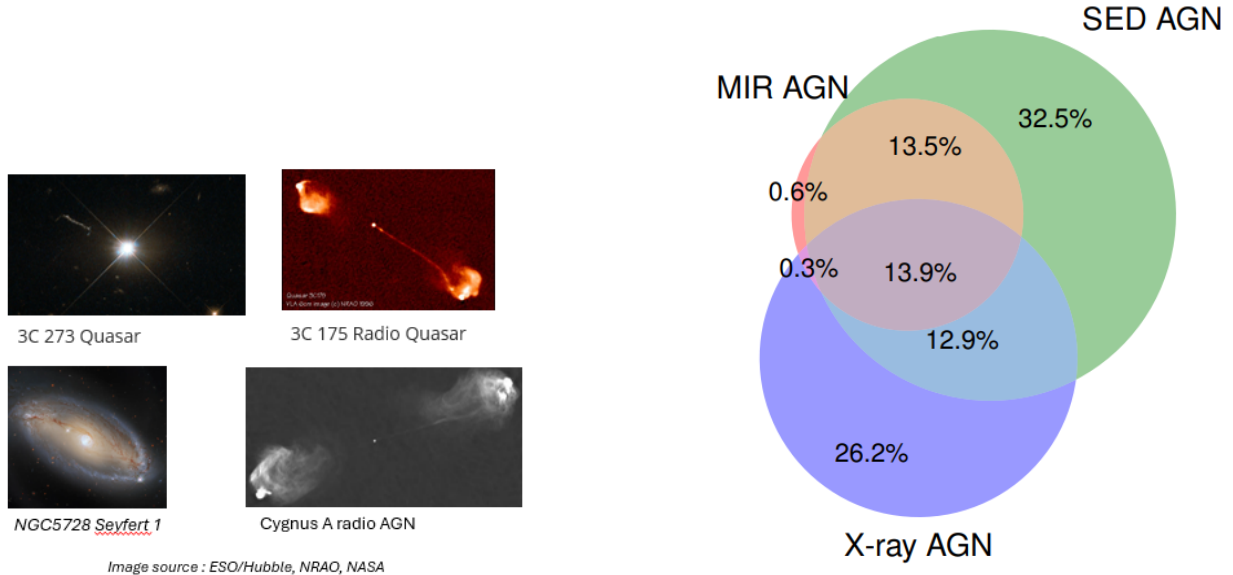
the energy balance approach typically applied to stellar populations. Unlike stellar emission, which is linked to star formation and follows predictable patterns, AGN emission originates from complex processes near the supermassive black hole, such as accretion and radiative transfer, making it harder to connect directly with the energy absorbed and re-emitted by dust.

1.2 Active Galactic Nuclei

Extremely luminous sources called quasars at high redshift were discovered first by [Schmidt \(1963\)](#), and this class is a part of the broad classification of galaxies having a compact central source and emitting across the whole or part of the electromagnetic spectrum, and are classified as AGN (Figure 1.2a). Their emission features indicate the heating of gas and dust by non-stellar sources. Some of these sources also exhibit high-energy radiation such as X-rays and gamma-rays. Several of the AGN identified later showed strong broad and narrow emission line features. Here broad emission features mean the emission lines with significantly higher velocity width relative to narrow lines, which arise from high-density gas clouds that move fast (1000 - 20,000 km/s), while the narrow line features have lower velocity width, arising from low-density cooler gas clouds moving at lower velocity (300 - 1000 km/s). The narrow lines seen in AGN are broader than those observed from ionised gas heated by stellar emission in normal galaxies. These features correspond to the broad line regions (BLR) and narrow line regions (NLR) associated with AGN and probe a crucial factor in the classification of AGN and understanding of the physical structure (Figure 1.3). The emission of non-thermal radiation in the radio and X-ray part of the spectrum by synchrotron emission and inverse Compton scattering is caused by the spiralling of relativistic electrons to a magnetic field, which is associated with compact regions and not with stellar emission. Considering the observations, the radiation source of an active galactic nucleus' central engine is believed to be a supermassive black hole that grows through the accretion of matter ([Rees, 1984](#)).

Some classes of AGN include but are not limited to, different quasi-stellar objects (QSO), radio galaxies, Seyfert galaxies and Low-Ionization Nuclear Emission-Line Regions (LINERs). QSOs are characterized by unresolved point-like luminous sources that are star-like. Here, the central source is extremely bright and often outshines the entire galaxy at most wavelengths. Seyfert galaxies are those with a central bright source of lower luminosity than QSO so that the host galaxy structure is more easily observed. Seyfert galaxies with both broad and narrow emission lines observed are classified as type 1 AGN, whereas those with only narrow emission lines are classified as type 2 AGN ([Netzer, 2015](#)). AGN are also classified by the presence or absence of radio emission, as radio-loud galaxies or radio-quiet. LINERs are a class of galactic nuclei characterized by their weak ionization emission lines, with spectra dominated by low-ionization elements such as [O I], [N II], and [S II], with lower luminosity than Seyfert galaxies ([Heckman, 1980; Ho et al., 1997](#)).

Observations show $\sim 3\%$ of the galaxy population are Seyferts (I and II) ([Hao et al., 2005a; Maia et al., 2003](#)), $\sim 3\%$ are radio-AGN ([Sabater, J. et al., 2019](#)) in the local universe. However,



(a) Different types of AGN observed. These include Quasar, Seyfert, Radio-Quasar, and Radio-loud AGN. Image credit : NASA/ ESO and the reference within.

(b) Venn diagram illustrating AGN selection types, highlighting that the methods are not fully complementary—AGN identified by one approach most often missed by others. source : [Delvecchio et al. \(2017\)](#)

Figure 1.2

the space density of quasars peaks at $z \sim 1.5$ and declines for higher redshift ([Hawkins & Véron, 1996](#)). In most of the studies, we see that the ‘AGN contaminants’ are removed using different selection methods, since the galaxy properties cannot be derived accurately in codes that do not include models for AGN emission. But here we extend our study to include AGN-host galaxies in SED fitting and deriving the galaxy properties effectively.

The Unified Model of AGN is the idea that the different types of AGN observed are the same type of source (i.e., the same physical mechanism), but are seen from different orientations or viewing angles (Figure 1.3; [Antonucci, 1993](#); [Urry & Padovani, 1995](#); [Padovani et al., 2017](#); [Netzer, 2015](#)). According to the Unified Model of AGN, the central emission source is an optically thick geometrically thin accretion disk where ionized gas and dust spiral into the black hole as an equatorial disk, heating up and emitting due to friction and high gravitational force of the black hole. A few to several parsecs away from the accretion disk are the spherically oriented dust-free gas clouds moving at high velocity and heated by the radiation from the accretion flow, the broad line region (BLR). Outside the BLR is a dust region as a toroidal structure that surrounds the AGN. The central accretion disk can be seen either directly or blocked by this dust torus, depending on the viewing angle of the source by the observer. The region that extends from outside the torus to several hundreds or thousands of parsecs is the narrow line region (NLR) constituting ionized gas and dust moving at lower velocity. The narrow lines observed are emitted from this region. Then, there is the radio jet on opposite sides, from the centre in a perpendicular direction to the accretion disk, caused by synchrotron emission. Type 1 AGN are observed when the BLR can be seen whereas in type 2 AGN the BLR is blocked by the torus. Similarly, radio-loud AGN are observed when the radio jet is seen

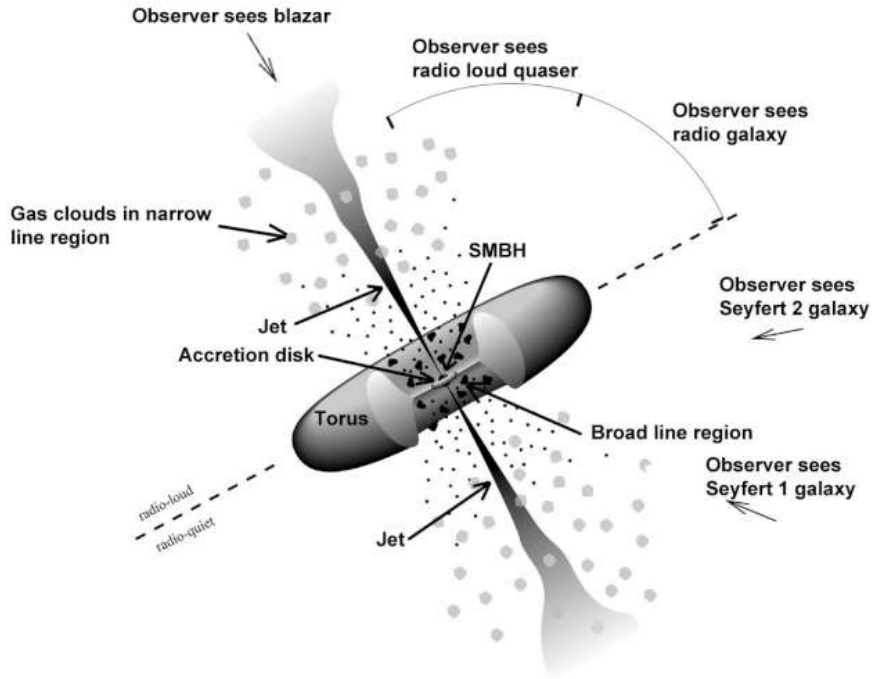


Figure 1.3: Representative cartoon illustrating the AGN unification model. The broad-line region (BLR) lies a few parsecs from the accretion disk, while the narrow-line region (NLR) is much farther away. A dusty torus obscures the accretion disk when viewed edge-on or from other high angles. Additionally, radio jets powered by synchrotron emission extend from the central black hole. The unification model suggests that the observed differences among AGN types arise primarily from variations in our viewing angle. The cartoon also shows how the different type of AGN are seen according to the different orientations. image source : [Urry & Padovani \(1995\)](#), credit: Robert Findlay

directly, while radio-quiescent are the ones where the radio jet is not directly seen.

Selection methods of AGN lie throughout the EM spectrum, mainly in X-ray, optical, IR, and radio regimes, due to the different physical processes that cause characteristic emission from AGN in these regions (Fig 1.2b). AGN selections often do not overlap because different methods target distinct AGN properties. These selection biases reflect the diversity in AGN environments and evolutionary stages, with some populations escaping detection in specific wavelengths due to obscuration or weak emission in certain bands ([Hickox et al., 2009](#); [Delvecchio et al., 2017](#)).

The physical mechanism behind the radio emission in AGN is the synchrotron emission. Synchrotron emission is caused by the acceleration of relativistic particles by a magnetic field. Major sources of synchrotron emission in galaxies are supernova remnants and central supermassive black holes. Comparatively strong radio emission by AGN is what distinguishes them so that they can be identified (Figure 1.4; [Padovani et al., 2015](#)).

The optical selection is another dependable AGN selection method, based on the observation of the broad and narrow line emissions that arise from the heating up of BLR and NLR by the accretion disk or from emission line ratios. The BPT diagram (Baldwin, Phillips & Terlevich) ([Baldwin et al., 1981](#); [Veilleux & Osterbrock, 1987](#)) is one of the most used tools to distinguish between star-forming galaxies and AGN by plotting specific emission line ratios, such as $[\text{O III}] \lambda 5007/\text{H}\beta$ vs. $[\text{N II}]\lambda 6584/\text{H}\alpha$. The elevated ionization levels of AGN lead to different

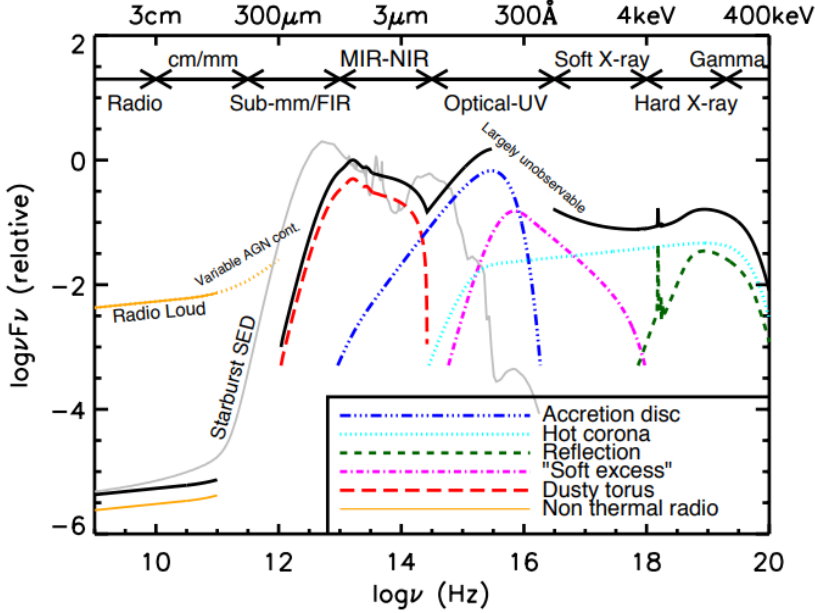


Figure 1.4: Schematic of the SED of an AGN, Image from [Padovani et al. \(2017\)](#), adapted from [Harrison et al. \(2014\)](#). The image shows the source of the spectrum and the different physical processes associated with it. This image was created by combining data from different observed active galaxies.

ratios of emission lines compared to ionization from young stars (this reflects differences in the X-ray spectral slope, with “hard” spectra having more high-energy photons and “soft” spectra dominated by lower-energy photons) and help to classify objects into Seyfert galaxies, LINERs, and star-forming. However, the optical emission can get absorbed if there is an obscuring dust torus between the source and the observer, making the identification of obscured AGN difficult. Hence optical selection is biased towards UV/optical-luminous, unobscured sources.

Inverse Compton scattering, where the UV and optical photons from the accretion disk are accelerated to X-ray wavelength by the relativistic electrons in the plasma around the accretion disk, is the primary process responsible for hard X-ray emission in AGN. Other sources of X-rays in galaxies are processes such as supernova explosion, X-ray binary emission, and emission from hot young stars. However, this host galaxy emission is mostly in the soft X-ray range, reducing the host-galaxy contamination in the X-ray selection of AGN ([Brandt & Alexander, 2015](#)). The ability of X-rays to penetrate through large column densities of gas and dust and the almost universality of X-ray emission from AGN makes X-ray selection more reliable. However, detecting Compton-thick (CT) AGNs—those surrounded by gas and dust with a column density $N_H > 1.5 \times 10^{24} \text{ cm}^{-2}$ ([Comastri, 2004](#))—is extremely challenging due to the heavy absorption of X-rays by dense material. However, the absorbed X-ray energy is often re-emitted in the IR providing an alternative method for the detection of AGN. Observational studies (e.g. [Brightman et al., 2014](#); [Ricci et al., 2015](#)) have confirmed the existence of CT AGNs through IR emission, complementing indirect X-ray evidence and their last fraction among AGN population ([Buchner et al., 2015](#)). The combination of multi-wavelength observations, especially in the IR, is essential for identifying and studying these highly obscured AGNs, which play a

critical role in understanding the growth and evolution of supermassive black holes.

The UV-optical obscured AGN population is as significant as the unobscured AGN (Hickox & Alexander, 2018). The mid-IR regime is another efficient way to identify and characterize the obscured AGN population (Laloux et al., 2022). The optical and X-ray photons absorbed by the dust will be emitted in IR wavelength. The mid-IR part gives a distinction between the dust heated by AGN and star formation (Puget & Léger, 1989; Allamandola et al., 1989) due to the temperature difference of the dust (\sim 30-50 K for SF-heated dust and \sim 200-1000 K for AGN-heated dust). Several color selections in IR wavelength have been developed (Lacy et al., 2004; Stern et al., 2005; Assef et al., 2013; Donley et al., 2012; Kirkpatrick et al., 2013) that separate AGN from star-forming galaxies. Even heavily obscured AGN can be identified since the selection method relies on emission from the obscuring dust. This method is also helpful in identifying AGN where the X-ray data are not available.

Integrating well-defined IR SEDs in multi-wavelength SED fitting is a useful tool in identifying and characterizing obscured AGN populations. The IR emission of a purely star-forming galaxy is closely linked to its star-formation rate (Kennicutt, 1998), while for extremely bright, dusty AGN it will be dominated by the dust torus. For cases in-between, the mid-IR emission can be linked with the total AGN activity (Horst, 2008) by decomposing the AGN and star-forming components of a composite galaxy (AGN+star forming) (Mullaney et al., 2011). Mid-IR emission due to star-forming radiation and AGN source differs physically in that dust can be heated to extremely high temperatures by the AGN source, giving rise to a power law such as emission in the mid-IR. Fig 1.5 shows the difference in the SED for varying levels of AGN contribution. At high AGN fraction, the SEDs appear to show a power-law till $\sim 20 \mu\text{m}$. In short, AGN templates can be implemented in SED fitting code so that the models with this AGN contribution can be compared to observational data. When the AGN components and star-forming components are separated in the IR, the relative AGN strength can be determined. The different stellar and dust properties can also be determined accurately after separating the AGN component from the total emission.

1.3 AGN Torus

The Unified Model distinguishes Seyfert 1 and Seyfert 2 by the absence or presence of obscuring dust torus between the AGN emission and observer. The detection of polarized light in Type 2 AGN, first by Antonucci & Miller (1985) serves as important evidence for the AGN unification model. The presence of silicate features is another evidence of the unification model. The $10 \mu\text{m}$ silicate feature arises due to the stretching modes of the Si-O bonds, and the $18 \mu\text{m}$ feature arises from the bending mode of O-Si-O, indicating the presence of silicate dust. Both these silicate features were observed as emission in type 1 AGN (Siebenmorgen, R. et al., 2005; Hao et al., 2005b), and as absorption in type 2 AGN (Jaffe et al., 2004). To predict and characterize the emission and absorption features of the torus, early works attempted modelling the torus as smooth dust distribution (eg: Pier & Krolik (1993)).

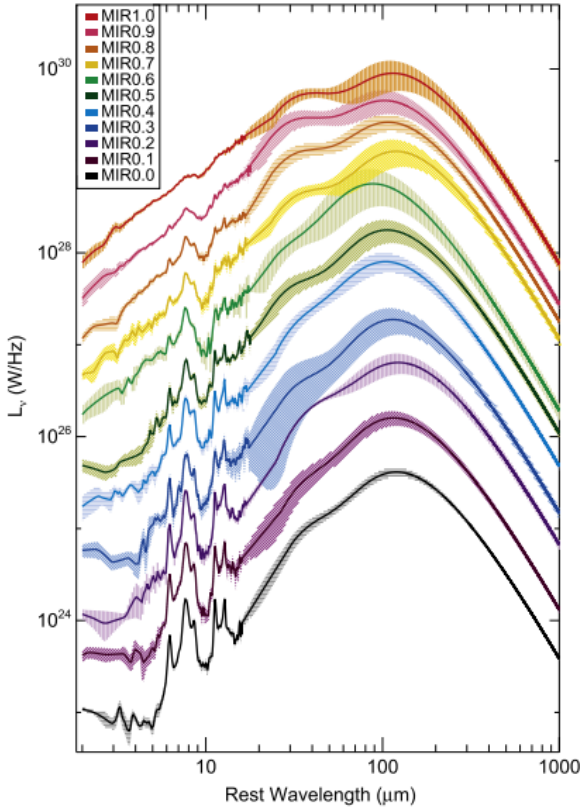


Figure 1.5: Change in SED for different levels of mid-IR AGN fraction in galaxies. MIR1.0 to MIR0.0 represent the 100 per cent to 0 per cent of AGN contribution templates. From [Kirkpatrick et al. \(2015\)](#)

Smooth models (e.g., [Fritz et al., 2006](#)) assume a continuous dust distribution within a toroidal shape, with density varying smoothly. While computationally simpler and useful for approximating the general shape of AGN IR emission, smooth models face several limitations: they predict silicate absorption features that are deeper than observed in Type-2 AGN, and rarely reproduce silicate emission in Type-1 sources ([Dullemond, C. P. & van Bemmel, I. M., 2005](#); [Feltre et al., 2012](#)). Furthermore, a smooth dust distribution is physically unrealistic, as it would lead to frequent dust collisions, heating the dust to destruction ([Krolik & Begelman, 1988](#)). Clumpy models, introduced by [Nenkova et al. \(2002\)](#), distribute dust in discrete clouds and better reproduce the broad IR bump and attenuated silicate features. However, clumpy models struggle to reproduce the short-wavelength emission from hot dust near sublimation temperatures, especially for Type-1 AGN ([Mor et al., 2009](#)). A more realistic approach is the two-phased torus model (e.g., [Stalevski et al., 2012](#); [González-Martín, Omaira et al., 2023](#)), which combines clumpy and smooth components. In this model, clumps represent discrete dust structures, preventing excessive heating, while the smooth component accounts for diffuse dust between the clumps, improving the fit to both the broad IR spectrum and short-wavelength emission. This hybrid model offers a more accurate and physically consistent representation of AGN dust emission.

We aim to replace the empirical AGN templates with torus emission templates which are created in a physically motivated way and backed by the mature Unified Model. Also, it is time

to move beyond the outdated empirical templates to the more robust torus emission models to explore the effects of key parameters, such as dust density and viewing angle, on the observed spectra. We adopted the [Stalevski et al. \(2012\)](#) two-phased tori model which will be explored in Chapter 4. We then compare the results of the new MAGPHYS version ‘MAGPHYS+AGN torus’.

1.4 Research Goal

The goal of this research is to investigate how the different galaxy physical parameters and dust parameters are calculated using the SED fitting process using MAGPHYS SED fitting code changes, with and without an AGN component. This will give insight into the need to implement the AGN component in the SED fitting code. We start with the already existing MAGPHYS version with AGN component implemented using 5 empirical AGN templates in the literature, which will be discussed later. Then we investigate how the addition of an AGN component will affect the SED fitting for normal/non-AGN galaxies. Finally, we explore how different the results of SED fitting are when Torus emission templates are used instead of empirical templates.

The thesis is organized as follows; Chapter 2 describes the data and methods used in this work. In Chapter 3, we show the main results of SED fitting with empirical AGN templates. In Chapter 4, we discuss the results of the implementation of torus emission templates in MAGPHYS+AGN. Then the conclusions and discussions are in Chapter 5. Throughout this work, we assume a Flat, Λ -Cold Dark Matter (Λ -CDM) Universe with $H_0 = 70 \text{ km s}^{-1} \text{ Mpc}^{-1}$, $\Omega_m = 0.30$, and $\Omega_\Lambda = 0.70$.

Chapter 2

Methods & Sample

2.1 MAGPHYS

The Multi-wavelength Analysis of Galaxy Physical properties (MAGPHYS, [da Cunha et al., 2008](#)) code uses an energy balance technique to analyze the observed galaxy spectra to interpret rest-frame UV to far-IR emission by combining stellar emission models with dust attenuation and dust emission models. The spectral evolution of stellar populations in galaxies is computed using the [Bruzual & Charlot \(2003\)](#) population synthesis technique that models the spectral evolution of stellar populations of different metallicities at ages between 1×10^5 and 2×10^{10} yr at wavelength range 9Å to 9500Å. The extinction and scattering of stellar emission passing through dust are modelled using the [Charlot & Fall \(2000\)](#) model. This model accounts for the interaction between stellar light and dust in two distinct components: the stellar birth clouds and the ambient ISM. In stellar birth clouds, which are regions where stars form, the dust tends to be denser, causing significant absorption and scattering of light, especially at shorter wavelengths. As stars age and move out of their birth clouds, the remaining light passes through the diffuse dust present in the ambient ISM, which has a lower density but still contributes to attenuation. By modelling these two components separately, the Charlot and Fall framework provides a more accurate description of how dust affects stellar emission over time, capturing both the initial heavy extinction in star-forming regions and the milder attenuation by the diffuse ISM throughout a galaxy. The total IR emission from dust is modelled by combining several components, each corresponding to different physical processes and dust populations emitting at various wavelengths. In the mid-IR region, the emission is dominated by polycyclic aromatic hydrocarbons (PAHs), which are complex molecules that absorb UV photons and re-emit energy in the IR. This emission is modelled using a modified blackbody function (or grey body) for accounting for the PAHs' non-ideal emissivity. Additionally, in the mid-IR, the emission from small, hot dust grains is modelled using a combined greybody function. This approach captures the continuum radiation emitted by these grains as they undergo stochastic heating events, where individual grains are sporadically heated by single photon absorptions to temperatures much higher than their equilibrium state. In the far-IR, the emission is attributed to warm and cold dust components. Grey body functions are employed to model these two

distinct populations, with warm dust emitting at shorter far-IR wavelengths and cold dust contributing more prominently at longer wavelengths. By combining a fixed template for mid-IR and grey body functions across the far-IR, the model provides a comprehensive representation of dust emission, capturing the contributions from both transiently heated small grains and the thermal emission from larger dust grains in a galaxy.

The stellar emission library that contains 25000 models is consistently combined with the 25000 models in the dust emission library. These models are compared with the observed galaxy data to get the best-fitting model having the lowest χ^2 value,

$$\chi^2 = \sum_{i=1}^N \left(\frac{f_{\text{obs},i} - f_{\text{model},i}}{\sigma_i} \right)^2, \quad (2.1)$$

where $f_{\text{obs},i}$ is the observed flux, $f_{\text{model},i}$ is the model flux and σ_i is the error.

The median likelihood of the physical parameters that best produce the stellar radiation and IR emission is given as output (stellar and dust parameters calculated by **MAGPHYS** are given in Table 4.1). The posterior likelihoods are calculated using a Bayesian formalism. The Bayesian approach defines a likelihood function that quantifies how well a given model explains the observed data, considering measurement uncertainties. Prior distributions are assigned to the model parameters based on prior knowledge or assumptions about their expected values. The fitting process then utilizes a brute-force approach where the data are compared against a fixed grid of models, generating posterior distributions that represent the updated probabilities of the model parameters given the observed data. This approach allows for robust estimation of physical properties, including uncertainties, and provides a systematic way to incorporate prior knowledge into the analysis.

The modified version of the SED fitting code **MAGPHYS highz** (da Cunha et al., 2015) includes SED fitting from the wavelength range of UV to Radio, and is suitable for galaxies of higher redshift ($z > 1$). This version of the code includes radio emission by applying the radio/far-IR correlation with fixed slopes for thermal and non-thermal components, following da Cunha et al. (2013). Thermal and non-thermal components refer to free-free emission from ionized gas and synchrotron emission from relativistic electrons, respectively. This version also incorporates more diverse star formation histories, extends the priors to higher optical depths, and includes additional dust attenuation parameters. It adds more IR emission models with a broader range of dust temperatures. The code is further updated to account for rest-frame UV absorption in high-redshift galaxies by applying the absorption prescription from Madau (1995). Since we are doing multi-wavelength SED fitting of high redshift galaxies ($z \sim 0 - 4$), we use **MAGPHYS highz** version as the standard version in this work and will be referred to as **highz**.

Chang et al. (2017) did SED fitting using **MAGPHYS highz+AGN emp**, a custom version of **MAGPHYS highz** that includes AGN component along with the stellar emission and dust emission libraries, to derive stellar masses, star formation rate, dust properties and AGN contribution of galaxies. They selected AGN in the COSMOS field (Scoville et al., 2007) by mid-IR power-law emission (i.e., using mid-IR color-color diagrams; see Section 2.3), to study the connection

Parameter	Description	Units
$f_\mu(\text{SFH})$	Fractional contribution of SFH to stellar mass	-
$f_\mu(\text{IR})$	Fractional contribution of IR emission to stellar mass	-
μ	Fraction of total IR luminosity from birth clouds	-
τ_V	Effective V-band optical depth (dust attenuation)	-
sSFR	Specific star formation rate	yr^{-1}
M_*	Stellar mass	M_\odot
L_{dust}	Total dust luminosity	L_\odot
T_W^{BC}	Dust temperature in birth clouds	K
T_C^{ISM}	Dust temperature in ISM	K
ξ_C^{tot}	Fractional contribution of cold dust to IR luminosity	-
$\xi_{\text{PAH}}^{\text{tot}}$	Fractional contribution of PAH to IR luminosity	-
$\xi_{\text{MIR}}^{\text{tot}}$	Fractional contribution of mid-IR continuum to IR luminosity	-
ξ_W^{tot}	Fractional contribution of warm dust to IR luminosity	-
τ_V, ISM	V-band optical depth in the ISM	-
M_{dust}	Dust mass	M_\odot
SFR	Star formation rate	$M_\odot \text{ yr}^{-1}$
A_V	V-band dust attenuation	mag
age_M	Mass-weighted age of the stellar population	Gyr
T_{dust}	Mass-weighted dust temperature	K
$\log(M/L_h)$	Stellar mass-to-light ratio in the H-band	$\log(M_\odot/L_\odot)$
$\log(M/L_k)$	Stellar mass-to-light ratio in the K-band	$\log(M_\odot/L_\odot)$

Table 2.1: MAGPHYS `highz` output parameters and their descriptions.

between AGN activity, star formation, and galaxy morphology. The galaxies were selected as AGN by defining a box similar to [Lacy et al. \(2004\)](#) and [Donley et al. \(2012\)](#) for monotonically rising IRAC band flux in the IRAC color space. The AGN templates used by [Chang et al. \(2017\)](#) in their work include SEDs for type-2 Seyferts ([Mullaney et al., 2011](#)), QSO ([Richards et al., 2006; Prieto, 2012](#)), and Seyfert 1 ([Polletta et al., 2007](#), AGN templates used are given in Figure 2.1). The AGN SED is combined with the stellar and dust emission libraries to create models to interpret the observed SED of galaxies. The best-fitting AGN template is decided from the lowest χ^2 model, which also tells the AGN type associated with the best-fitting AGN template. The total dust emission in the IR (3-1000 μm) is divided as dust luminosity by star formation ($L_{\text{dust}}^{\text{SF}}$) and dust luminosity contributed by AGN ($L_{\text{dust}}^{\text{AGN}}$), by subtracting the AGN SED from the total dust luminosity of the model. The PDF and best-fitting values of these luminosity parameters are also calculated in `AGN.emp`. For each model, a contribution of dust heated by the AGN is also measured by calculating ξ_{AGN} parameter, which is the fraction of the dust heated by the AGN in the IR wavelengths to the total dust heated luminosity (by the following equation)

$$\xi_{\text{AGN}} = L_{\text{dust}}^{\text{AGN}} / (L_{\text{dust}}^{\text{SF}} + L_{\text{dust}}^{\text{AGN}}) . \quad (2.2)$$

The pdf and best-fitting values of ξ_{AGN} are also calculated by the code. ξ_{AGN} has a flat prior from 0 to 1, meaning any value is equally likely. ξ_{AGN} is the normalization factor that fits the AGN component to the observed IR emission. A higher value of ξ_{AGN} indicates that the AGN

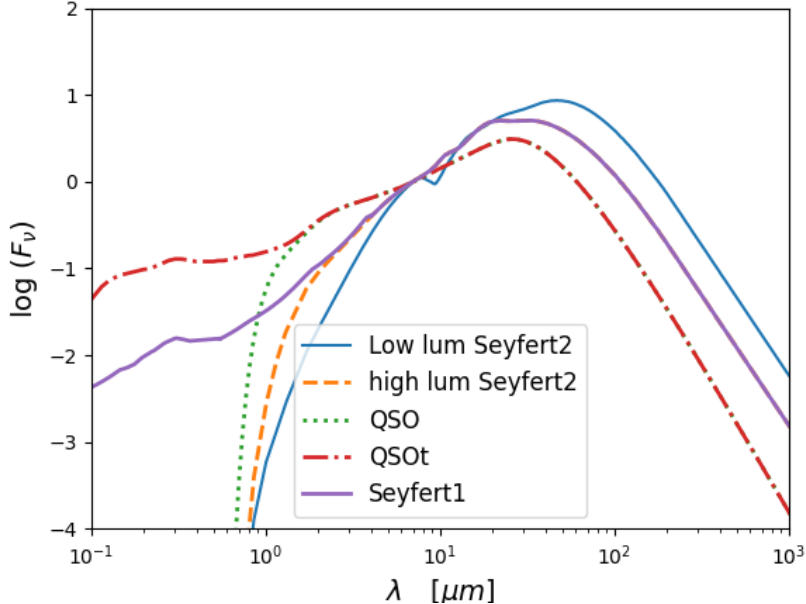


Figure 2.1: representative empirical AGN templates used in MAGPHYS highz+AGN emp version (Chang et al., 2017)

powers a larger fraction of the dust emission in the IR, while a lower value suggests that star formation is the dominant heating source. This parameter helps disentangle the contributions of AGN and stellar processes to the total IR luminosity, ensuring that the SED fitting accurately reflects the physical properties of both components.

The Seyfert 2 templates (low luminosity and high luminosity) are adopted from Mullaney et al. (2011) which are derived intrinsic AGN IR SED by removing host galaxy components from a set of local X-ray AGN in the *Swift*-BAT survey (Tueller et al., 2008) with minimal contamination from host galaxies in MIR spectra. The Seyfert 1 template was adopted from Polletta et al. (2007) who derived the average SED of hard X-ray selected AGN sources with photometry from X-ray, UV, and IR photometry in the XMM-Newton Medium Deep Survey (Chiappetti et al., 2005) by template fitting. The QSO (Richards et al., 2006) and QSOT (Prieto, 2012) templates differ by the broad emission lines at optical wavelength being included in the latter.

2.2 COSMOS2020 catalogue

We compare the results of SED fitting for a sample of AGN candidate galaxies for codes with an AGN component (MAGPHYS highz+AGN emp version) and without the AGN component (highz version). Potential AGN candidates were selected using 3 color-color separation methods described in Section 2.3.

We use the COSMOS survey (Capak et al., 2007; Scoville et al., 2007) for selecting AGN, as its 2 deg² field provides deep multi-wavelength photometric and spectroscopic data, including mid-IR and far-IR photometry from *Spitzer*/IRAC and *Herschel*, along with sub-millimetre,

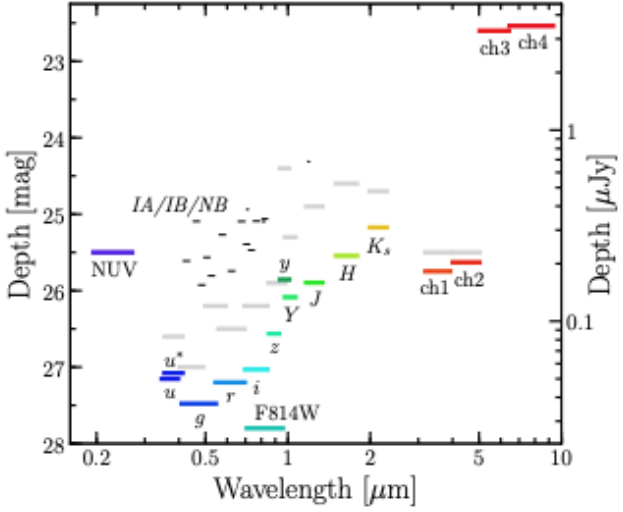


Figure 2.2: Depth of the various photometric bands in the COSMOS2020 survey (Weaver et al., 2022) within the COSMOS field. The F814W band provides the deepest data in the survey. Among the *Spitzer*/IRAC bands, ch1 and ch2 reach greater depths compared to ch3 and ch4.

radio observations, and spectroscopic redshifts for numerous galaxies, making it ideal for our research. Availability of spectroscopic redshift is important for the SED fitting in our work, since the library of stellar and IR colors are computed by the MAGPHYS versions used in this work are dependent on accurate redshift given as input. (However the MAGPHYS+photoz (Battisti et al., 2019) version of the code calculates the photometric redshift of galaxies, but we are not using this version in this work).

The latest photometric release of the COSMOS field, the COSMOS2020 catalogue (Weaver et al., 2022), provides UV through mid-IR photometry from *GALEX*, CFHT, Subaru, UltraVista, and *Spitzer*/IRAC telescopes. This was combined with the Super-deblended photometry catalogue (Jin et al., 2023), which extends the wavelength coverage of COSMOS sources for the mid-IR through radio wavelength range from the *Spitzer*/MIPS, *Herschel*, SCUBA-2, AzTEC, MAMBO, and Very Large Array telescopes. The cross-matching relies on the COSMOS2015 catalogue ID columns, which remain consistent across both catalogues (i.e., the nearest source in the COSMOS2015 catalogue, Laigle et al., 2016).

Out of the 704,083 objects in the ‘FARMER catalogue’ of COSMOS2020, we select a sub-sample with spectroscopic redshifts (21,767). Even though photometric redshifts computed by EAZY (Brammer et al., 2008) and LePhare (Arnouts et al., 2002; Ilbert, O. et al., 2006) codes are available in the catalogue, spectroscopic redshifts were used for their better accuracy than the former. The spectroscopic redshifts were from curation by M. Salvato for internal use within the COSMOS collaboration.

2.3 Sample Selection

Here we discuss how the potential AGN candidates are selected using the different IR color-color cut, along with the galaxies in the control sample galaxies are selected.

2.3.1 *Spitzer*/IRAC selection

First, the *Spitzer*/IRAC selection defined by [Donley et al. \(2012\)](#) was used to separate AGN from the parent spectroscopic sample. For the star-forming galaxies, PAH features are seen in the mid-IR wavelength and there would be a dip between the $1.6\ \mu\text{m}$ stellar bump and IR emission from dust heated by star formation. However, for AGN the dust will be heated to high temperature and the continuum would appear to be power-law-like. These differences in near-IR SED shape can be separated in the color-color space of IRAC bands. The [Donley et al. \(2012\)](#) selection criteria are as follows, where \wedge is the logical “AND” operator:

$$\begin{aligned} x &= \log_{10}\left(\frac{f_{5.8\mu\text{m}}}{f_{3.6\mu\text{m}}}\right) \quad , \quad y = \log_{10}\left(\frac{f_{8.0\mu\text{m}}}{f_{4.5\mu\text{m}}}\right) \\ x \geq 0.08 \quad &\wedge \quad y \geq 0.15 \\ \wedge \quad &y \geq (1.21 \times x) - 0.27 \\ \wedge \quad &y \leq (1.21 \times x) + 0.27 \\ \wedge \quad &f_{4.5\mu\text{m}} > f_{3.6\mu\text{m}} \wedge f_{5.8\mu\text{m}} > f_{4.5\mu\text{m}} \wedge f_{8.0\mu\text{m}} > f_{5.8\mu\text{m}} . \end{aligned} \tag{2.3}$$

Equation 2.3 includes the power-law box that defines AGN-dominated sources within the color space. Luminous AGNs typically follow a power-law slope of $\alpha < -0.5$ (up to -3.0 in this selection criteria) for $f_\nu \propto \nu^\alpha$, where f_ν is the monochromatic flux density and ν is the frequency. This relationship indicates that as the frequency increases (or wavelength decreases), the flux density decreases, resulting in a power-law increase of flux with increasing IRAC filter wavelengths.

The $x \geq 0.08$ line excludes the low-redshift star-forming galaxies, while the $y \geq 0.15$ line excludes high-redshift star-forming galaxies. The selection criteria ensure the monotonic rise of IRAC SEDs. We selected only those galaxies with $S/N(\text{IRAC}) > 3$ for reliable data. The IRAC selection criteria were applied to these galaxies and 142 AGN candidates were selected, this is our ‘IRAC AGN’ sample (Figure 2.3). The galaxies in the IRAC AGN sample have a median redshift ≈ 1.67 , with the highest ≈ 3.85 and lowest ≈ 0.03 (Figure 2.4).

However, this selection criterion effectively identifies luminous, obscured AGNs in the IRAC bands but tends to miss low-luminosity AGNs. Moreover, at $z > 3$ star-forming galaxies may contaminate the AGN sample. Further, this selection criteria depends on all four *Spitzer*/IRAC bands being available. The COSMOS2020 catalogue has shallower depth in the IRAC-3 and IRAC-4 bands compared to IRAC-1 and IRAC-2 (see Figure 2.2). This is because IRAC-1 and IRAC-2 were observed to greater depth during the *Spitzer* telescope’s extended ‘Warm

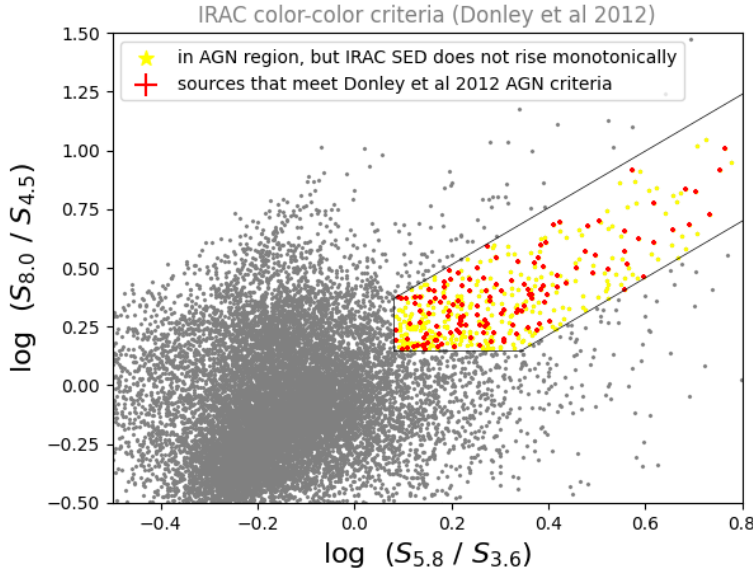


Figure 2.3: IRAC color selection. The red points are the galaxies selected as IRAC AGN samples while the yellow points are the galaxies that are within the region but whose IRAC SEDs do not rise monotonically. The grey points are the galaxies having $S/N > 3$ for IRAC1,2,3,4 bands.

Mission¹, which collected data for several additional years. To account for the missing IRAC-3 or IRAC-4 data, we employ an alternative infrared color-selection method that combines IRAC-1 and IRAC-2 with *Herschel* bands to identify AGN.

2.3.2 *Spitzer+Herschel* color cut

Next, we looked into *Spitzer+Herschel* color cut diagnostics prescribed by Kirkpatrick et al. (2013) to separate AGN from high redshift galaxies ($0.5 < z < 4$). They combined near-IR with mid- and far-IR bands to distinguish AGN from star-forming galaxies in the color space of S_{250}/S_{24} vs $S_8/S_{3.6}$ and S_{100}/S_{24} vs $S_8/S_{3.6}$. AGN can be selected by:

$$\log(S_8/S_{3.6}) > 0.74 \times \log(S_{250}/S_{24}) - 0.78. \quad (2.4)$$

We applied the above color cut to galaxies in our COSMOS sample with $S/N > 3$ in S_{250} , S_{24} , S_8 , and $S_{3.6}$, redshift in the range 0.5-4, and obtained 25 galaxies, which goes to our *Spitzer/Herschel* AGN sample (Figure 2.5). In this sample, we expect both silicate-featured AGN and featureless AGN. Silicate AGN is the absorption at $9.7 \mu\text{m}$, whereas featureless AGN is characterized by just a power-law in the IRAC bands. In the absence of SPIRE250 data, the separation between AGN and SF galaxies can be done by substituting S_{100} for S_{250} :

$$\log(S_8/S_{3.6}) > 0.208 \times \log(S_{100}/S_{24}) + 0.105. \quad (2.5)$$

¹*Spitzer* Warm and Cold missions overview: <https://www.spitzer.caltech.edu/mission-mission-overview>.

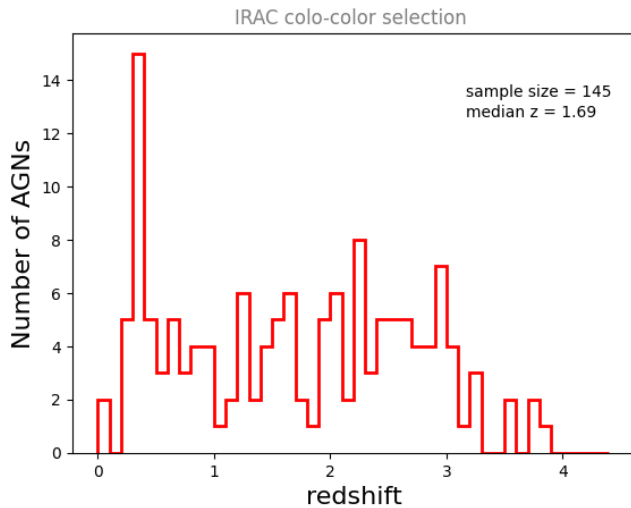


Figure 2.4: redshift distribution of galaxies in IRAC AGN sample. Galaxies are distributed across the redshift between $\approx 0 - 3.85$

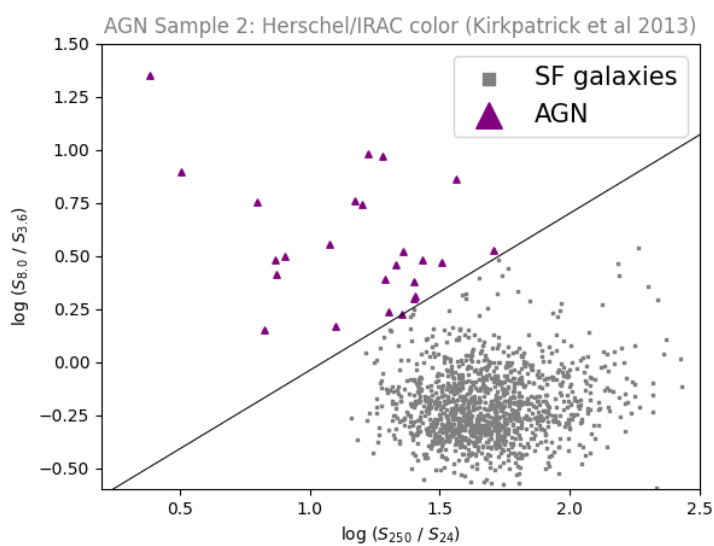


Figure 2.5: AGN selected using colorcut prescribed in [Kirkpatrick et al. \(2013\)](#). The blue triangles are the galaxies that fall in the AGN color space and go into the *Spitzer/Herschel* AGN sample

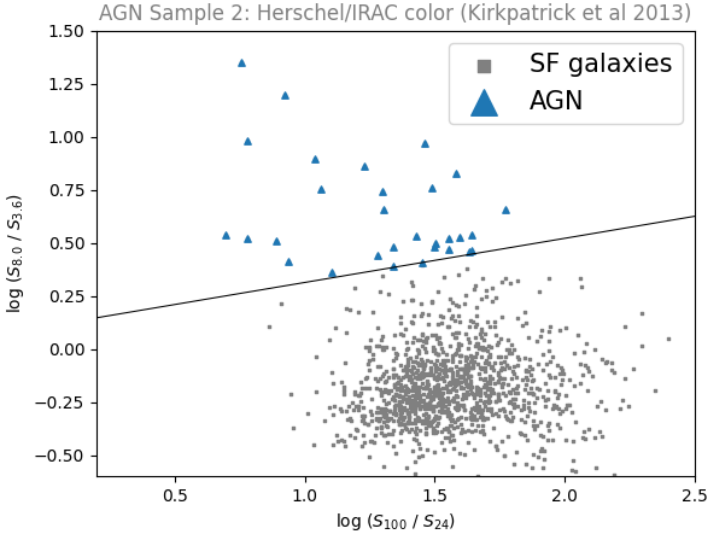


Figure 2.6: AGN selected using color cut prescribed in [Kirkpatrick et al. \(2013\)](#). The blue triangles are the AGN selected and the grey dots are galaxies in the COSMOS sample with spectroscopic redshift and having $S/N > 3$ in IRAC1, IRAC4, MIPS24, and SPIRE100 bands.

Galaxies at $z > 0.5$ were distinguished as AGN by applying the above cut to get 30 galaxies which goes to the ‘*Spitzer/Herschel* AGN’ sample (Figure 2.6). There are 16 common galaxies in the 2 color cuts done above and sampled as *Spitzer/Herschel* AGN samples. The combined *Spitzer/Herschel* AGN sample has 39 galaxies with redshift in the range ~ 0.5 to 3.5 (Figure 2.7). Most of the galaxies in this sample are in $0.5 < z < 1$, and only a few galaxies between redshift 2 and 3.5. The lower number of AGN found in this color cut, compared to the IRAC color-color criteria, was because of the shallow data available for the *Spitzer/MIPS* (24 μm) and *Herschel* (100 μm , 250 μm) compared to the *Spitzer/IRAC* data.

2.3.3 Radio loud sources

Next, a sample of galaxies was selected based on the radio ($S_{1.4\text{GHz}}$) to near-IR (S_{K_s}), and mid-IR ($S_{24\mu\text{m}}$) flux density ratios ([Driver et al., 2018](#); [Seymour et al., 2008](#)). The IR and radio selection methods select different AGN populations so that we get a broader AGN population. We select these AGN candidates using radio-selection methods to see how the results of the SED fitting differ for them as we characterize the obscured AGN in `AGN.emp`.

$$\log(S_{1.4\text{GHz}}/S_{K_s}) > 1.5 \quad (2.6)$$

$$\log(S_{24\mu\text{m}}/S_{1.4\text{GHz}}) < 0.0 \quad (2.7)$$

Eq ?? identifies sources where the radio emission is significantly stronger than the stellar emission (seen in K_s band). The radio selection of AGN relies on their deviation from the IR-radio correlation typically observed in star-forming galaxies ([Condon, 1992](#); [Yun et al., 2001](#)). In star-forming galaxies, radio and IR emissions are tightly correlated because both originate from processes related to star formation, such as synchrotron emission from supernovae and

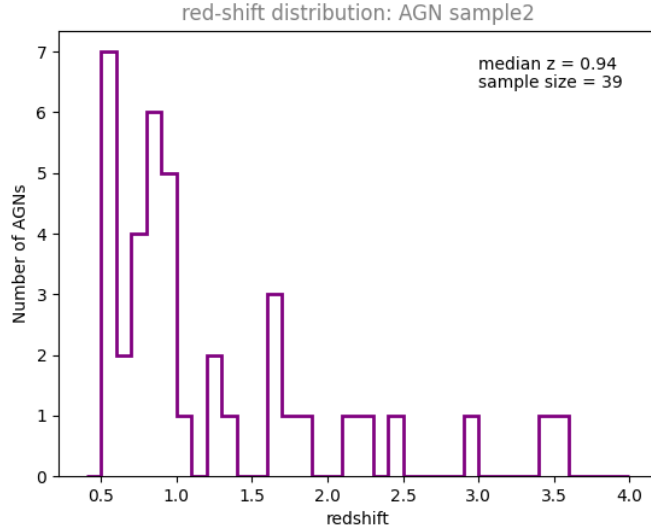


Figure 2.7: redshift distribution of *Spitzer/Herschel* AGN sample

thermal emission from dust heated by young stars. However, AGN often exhibits excess radio emission, breaking this correlation, as their radio output is dominated by relativistic jets and lobes powered by the central supermassive black hole, rather than star formation. Galaxies that come under either of the conditions eq 2.6 or eq 2.7 are selected as radio-loud sources. 276 galaxies satisfy this selection criterion and are sampled as a ‘radio-loud AGN’ sample (Figure 2.8).

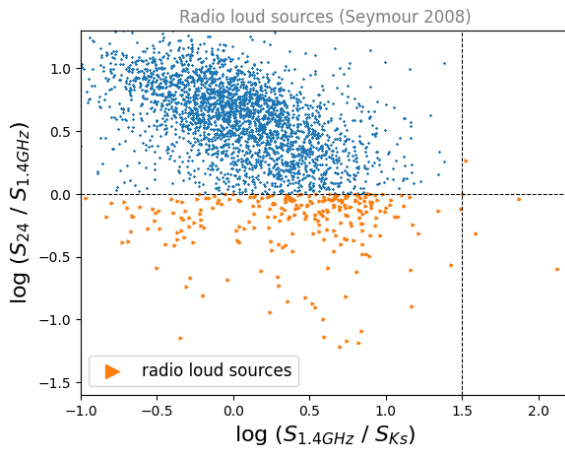


Figure 2.8: Radio loud sources separated using methods from Seymour et al. (2008). The orange color dots are the Radio-loud AGN sources, and the blue dots are the other sources in the COSMOS sample.

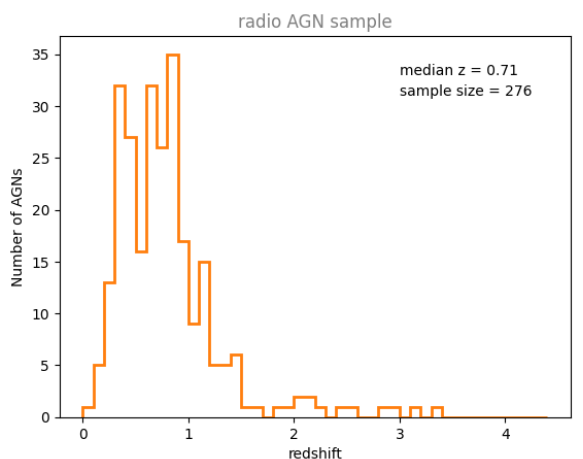
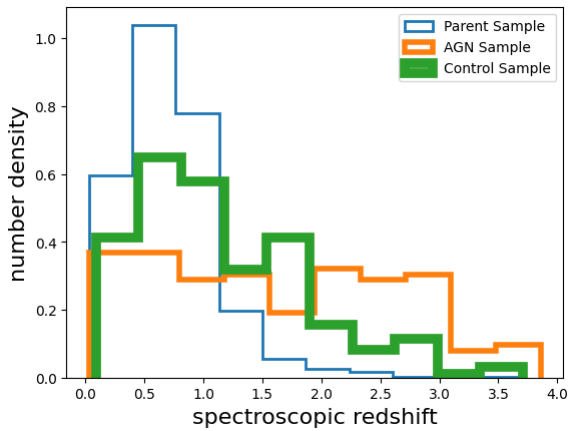


Figure 2.9: redshift distribution of radio sampled AGN. Most of the galaxies are in the redshift range of 0.2 to 1.5

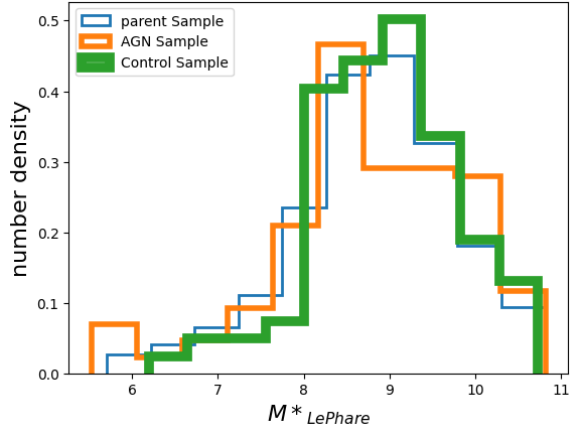
The galaxies in the radio-loud AGN sample are in the redshift range ~ 0.08 and 3.3 (Figure 2.9). The major population resides in the redshift range of 0.2-1.5.

2.4 Control sample

A control sample was created by selecting galaxies with comparable properties to those in AGN samples. This is to check how `MAGPHYS highz+AGN emp` version can fit galaxies that are not AGN. We need to see how the AGN fraction of the galaxies in the control sample are, and see if the physical properties derived using `highz` changes if the AGN component is added to the fitting process. Ideally, we want the AGN version to not introduce any biases on galaxies with no AGN component. To select galaxies for the control sample, all the galaxies in the AGN samples were removed from 21,767 COSMOS spectroscopic parent sample of galaxies. First cut was done by selecting galaxies having $S/N > 3$ for $S_{3.6\mu m}$, $S_{4.5\mu m}$, $S_{5.4\mu m}$, $S_{8.0\mu m}$ and ($S_{24\mu m}$ or $S_{250\mu m}$ or $S_{100\mu m}$). These are the bands we used for the IR AGN selection using color cuts. A strict cut for the flux in all the 24 μm , 100 μm , and 250 μm bands was not implemented to avoid bias because data in these higher wavelength bands may not be available, compared to the IRAC bands. Next, we applied redshift and stellar mass (M_*) cut to the above sample and found 8596 galaxies. The prior information on M_* was obtained from the COSMOS2020 catalogue (Weaver et al., 2022), calculated using `LePhare` code. From this, a random sample of galaxies (180) were selected. But we can see that the number of high redshift galaxies in the parent sample is really low (Figure 2.10a). So, we select random galaxies of $z > 1.5$, and all galaxies of $z > 2.5$ to ensure the completeness of the redshift range as similar to the AGN sample. This makes the final ‘Control’ sample with 239 galaxies.



(a) Redshift distribution.



(b) Stellar mass distribution.

2.5 SED fitting

The procedure to perform SED fitting using `MAGPHYS highz` is explained here briefly. The filter information (including the filter band name and effective wavelength) for all the filter bands for which multi-wavelength SED fitting needs to be done, along with the galaxy ID, redshift, and observed flux and error for all the bands are given as input as an ASCII table. For each redshift, the code creates a stellar emission library and an IR emission library with stellar and dust parameters respectively, along with colors for the filters used. The main code is then run

to obtain the best-fitting SED along with its galaxy parameters. The probability distribution function (PDF) of the different stellar and dust parameters is computed and their percentiles are also calculated by the fitting code.

The difference between `highz` and the custom `MAGPHYS+AGN emp` is the addition of the ‘AGN emission’ library along with other libraries computed for each redshift. The main fitting code is also different for this version.

The filter bands used for the multi-wavelength SED-fitting process for ‘IRAC AGN’ sample, ‘*Spitzer/Herschel* AGN’ sample and the control sample are given in Table 2.2. For the ‘Radio AGN’ sample, the 10 cm and 20 cm band data of Very Large Array radio telescope, from ‘Superdeblended catalogue ([Jin et al., 2023](#))’ was also added for the SED fitting along with bands in Table 2.2. This is done to ensure radio data for the radio-selected AGN sample galaxies.

FILTER	Effective Wavelength
GALEX FUV	0.1526
GALEX NUV	0.2307
CFHT u	0.3709
CFHT u*	0.3858
HSC g	0.4847
HSC r	0.6219
HSC i	0.7699
HSC z	0.8894
HSC y	0.9761
UVISTA Y	1.022
UVISTA J	1.252
UVISTA H	1.647
UVISTA Ks	2.156
IRAC CH1	3.569
IRAC CH2	4.507
IRAC CH3	5.779
IRAC CH4	7.996
MIPS 24	23.67
PACS 100	101.4
PACS 160	163.6
SPIRE 250	249.3
SPIRE 350	349.9
SPIRE 500	504.1
SCUBA 850	863.3
AZTEC 1100	1130
MAMBO 1200	1200

Table 2.2: Filters used in the SED fitting throughout the project, for galaxies from COS-MOS2020 catalogue

Chapter 3

Results

3.1 MAGPHYS highz vs MAGPHYS highz+AGN emp

Multi-wavelength spectral energy distribution fitting was done for all galaxies in the 3 AGN samples and the control sample, first using `highz` and then using `AGN emp`. The fitting results and comparison of a single galaxy will be illustrated first. The results of the whole sample will be discussed in the later sections. Fig 3.1 shows the SED fitting done for a galaxy in the *Spitzer/Herschel* AGN sample using `highz`, and in Figure 3.2 we see the fitting results of the same galaxy done with `AGN emp`. The best-fitting template can be used to classify the galaxy as which AGN type it belongs to. This is useful for galaxies having a high AGN contribution, but this cannot be considered reliable for low AGN fraction galaxies because adding a negligible amount of emission from any of the templates can provide an equally good fit if an AGN component is not required in the SED. Comparing the two plots, the fitting of data became better in the mid-IR region with an AGN component, particularly in the $5.8\mu\text{m}$ and $8.0\mu\text{m}$ bands. An exception in the IR is the $250\mu\text{m}$ band, which does not fit well in both models. The improvement in the fitting can also be seen in the lower value of χ^2_{red} . We expect the χ^2_{red} to be lower when fitted using a more flexible model, as in here 5 AGN templates were added, increasing the number of models available to fit the data (i.e., there are more free parameters).

Next, we explore the AGN fraction of the galaxy, which is the ξ_{AGN} value determined using the AGN templates. After considering the errors, the galaxy in Figure 3.2 shows more than 50 percent dust heated by an AGN source and the ξ_{AGN} PDF is also fairly constrained. The SED is consistent with the power-law-like shape seen in the IRAC bands, which is a signature of the central nucleus heating the dust. The low luminosity Seyfert 2 template is the best-fitting result for this galaxy. These galaxies are characterized by significant dust emission in the IR.

Next, we look at the physical parameters of this galaxy, some of the parameters like star-formation rate and ISM-optical depth have significantly decreased when fitted with the AGN component. Without the AGN component, all the dust heated was assumed to be from star formation, and more star formation was needed for the total dust luminosity. However, the central AGN contribution can reduce the overestimation of SFR. In short, this galaxy shows a high AGN fraction in the IR region, along with drastic changes in derived parameters.

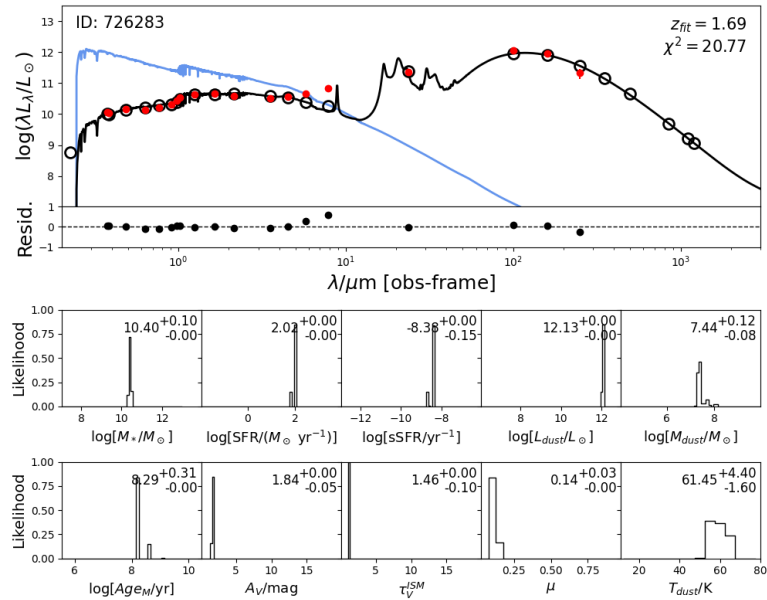


Figure 3.1: SED fitting result of a galaxy in *Spitzer/Herschel* AGN sample, using `highz`. The top panel is the SED of the galaxy, where the light-blue line is the un-attenuated SED which is the original emission from the galaxy entirely contributed by star formation. The black line in this panel is the total fit SED which is the emission after the flux reprocessed by dust in the ISM and stellar birth clouds. The red dots in the panel are the observed flux, while the black circles are the model flux. The second panel in the plot is the residual plot which shows the deviation of observed data from model data. The PDF of the physical parameters of the galaxies with the errors is also plotted in the lower panels. We can see that the mid-IR bands are not fitted well, which is reflected in the high χ^2 value.

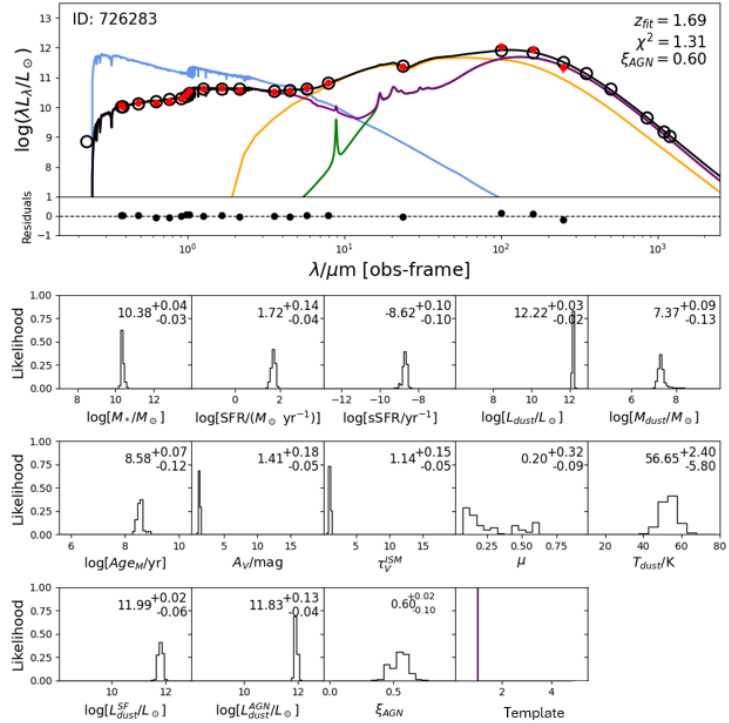


Figure 3.2: SED fitting results of the same galaxy with AGN `emp`. The orange line is the AGN component, the green line is the dust luminosity heated by star formation, purple line is the fit without the AGN component. Additional parameters and their PDF are plotted in the figure, such as dust luminosity by star-formation (L_{dust}^{SF}), luminosity of dust heated by AGN (L_{dust}^{AGN}), AGN fraction in the IR dust luminosity (ξ_{AGN}), and additionally the best-fitting AGN template. The fit improved, which is reflected in the lower χ^2 value. The ξ_{AGN} value given in the top panel is the 50th percentile of the PDF. This galaxy has a high AGN fraction in the IR luminosity.

3.1.1 χ^2 comparison

The reduced- χ^2 (χ_{red}^2) is a measure of how well a model fits the observed dataset, adjusted for the number of data points and the number of parameters in the model. However, the χ_{red}^2 calculated by different versions of MAGPHYS code is normalized by the total number of filters used for the SED fitting process (i.e., $\chi_{red}^2 = \chi^2/\text{number of filters}$). This convention is widely adopted in SED modelling codes because the complexity of models and templates makes it difficult to reduce them to a fixed set of independent parameters. The numerous degeneracies—where multiple combinations of galaxy parameters produce similar SED colors—complicate the process, preventing a straightforward parameterization. Since we use the same (number of) filters for the fitting process of the samples in both versions of the code, we can compare how the χ_{red}^2 changes for the galaxies when fitted with and without the AGN component. Ideally, $\chi_{red}^2 = 1$ for a good fit, and closer to 1 are reasonable fit. $\chi_{red}^2 < 1$ indicates the over-fitting of data (model fits the noise), and $\chi_{red}^2 \gg 1$ indicates poor fit.

We show the comparison of χ_{red}^2 derived from the code for `highz` vs `emp` in Figure 3.3 and find that there are many galaxies with $\chi_{red}^2 \gg 1$ when fitted with `highz`, which indicates the missing components or bad assumption in the model since these are AGN candidate galaxies. We find the χ_{red}^2 calculated by the code decreases when fitted with AGN `emp`. This is the expected result, as the addition of the AGN component makes the model more flexible since the number of models increases showing the necessity of adding an AGN component in the model while fitting galaxies having an AGN component. However, a lower value of χ_{red}^2 is not necessarily an indication of a better model but suggests more flexibility to fit the data. To ensure the reliability of the AGN contributions, we will independently verify the ξ_{AGN} values derived from MAGPHYS by comparing them with empirically derived values obtained from mid-IR spectroscopy (see Section 4.2). That can be evident from the fact that the galaxy with the highest value of χ_{red}^2 when fitted without an AGN component is still the galaxy with the highest value of χ_{red}^2 when fitted with the AGN component. We also see that a vast number of galaxies have $\chi_{red}^2 \gg 1$ even when fitted with the AGN components. Also, as the number of models increased, the fitting code might start to fit the noise, which is referred to as overfitting, and this could have happened for that one galaxy for which the χ_{red}^2 increased when fitted with AGN `emp`. We can look into how these results change when even more flexibility is given to the model, in the later sections. Other reasons for the bad fits may be due to the bad quality of data (noise) for the IR wavelength data from the Super-deblended catalogue.

3.1.2 Band-wise residual

Next, we look into how each filter band is fitted to the data by calculating the residuals ((observed flux - model flux)/error) of them individually. Ideally, the distribution of the residuals should obey a Gaussian centred at $\mu = 0$ and a standard deviation $\sigma = 1$. The probability density of residuals for 9 bands is shown in Figure 3.4 for the IRAC and *Spitzer/Herschel* AGN samples combined. It's evident that the AGN component significantly improves the residuals for K,

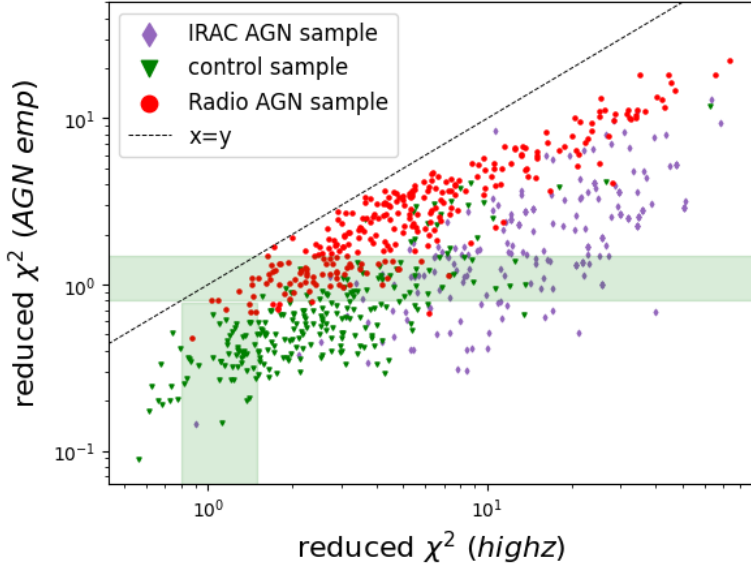


Figure 3.3: The χ_{red}^2 decreases when the AGN component is added, suggesting flexibility to the model. However, there are still a lot of galaxies with $\chi_{red}^2 \gg 1$. The galaxies with χ_{red}^2 near 1 (0.8 to 1.5) when fitted with `emp` are in the green shaded region, which can be considered good fits.

IRAC2, IRAC4, and MIPS24 bands. Also, all of them (except, the IRAC 1 band) mostly follow a Gaussian centered at 0, but the deviation seems higher. This shows that these bands are fitted well with an AGN component. However, the IRAC1 band seems to be dragged towards the positive side with the AGN `emp`, indicating the underestimation of the observed data. This may suggest a limitation of the stellar models, as the near-IR range is more uncertain than the UV-optical range in terms of the uncertain contribution of evolved stars (e.g., giants([Conroy, 2013](#))). The residual vs redshift for the same bands (Figure 3.5) shows the improvement in fitting for the MIPS24 band at $z > 1.5$, and at $z \approx 1.5$ for the IRAC4 band. However, the low sample size at the high redshift end might bias the results.

3.1.3 ξ_{AGN} distribution

Dust luminosity heated by star formation (L_{SF}^{dust}) and dust luminosity heated by AGN (L_{AGN}^{dust}) are separated for galaxies while fitted using AGN `emp`. The ξ_{AGN} parameter is also calculated in the code which gives the fraction of AGN contribution in the dust-heated luminosity at $3 - 2000 \mu\text{m}$,

$$\xi_{AGN} = \frac{L_{dust}^{AGN}}{(L_{dust}^{AGN} + L_{dust}^{SF})}. \quad (3.1)$$

Galaxies can have low to medium to high amounts of AGN contribution. It would be reasonable to argue that a galaxy can have an active nucleus if it has at least a 10 percent AGN contribution within the errors in its spectra. We expect IR-selected AGN with high AGN contribution to have a high value of ξ_{AGN} since the dust near the accretion disc will be heated to high temperature giving rise to high luminosity in the IR region. The probability distribution function (PDF)

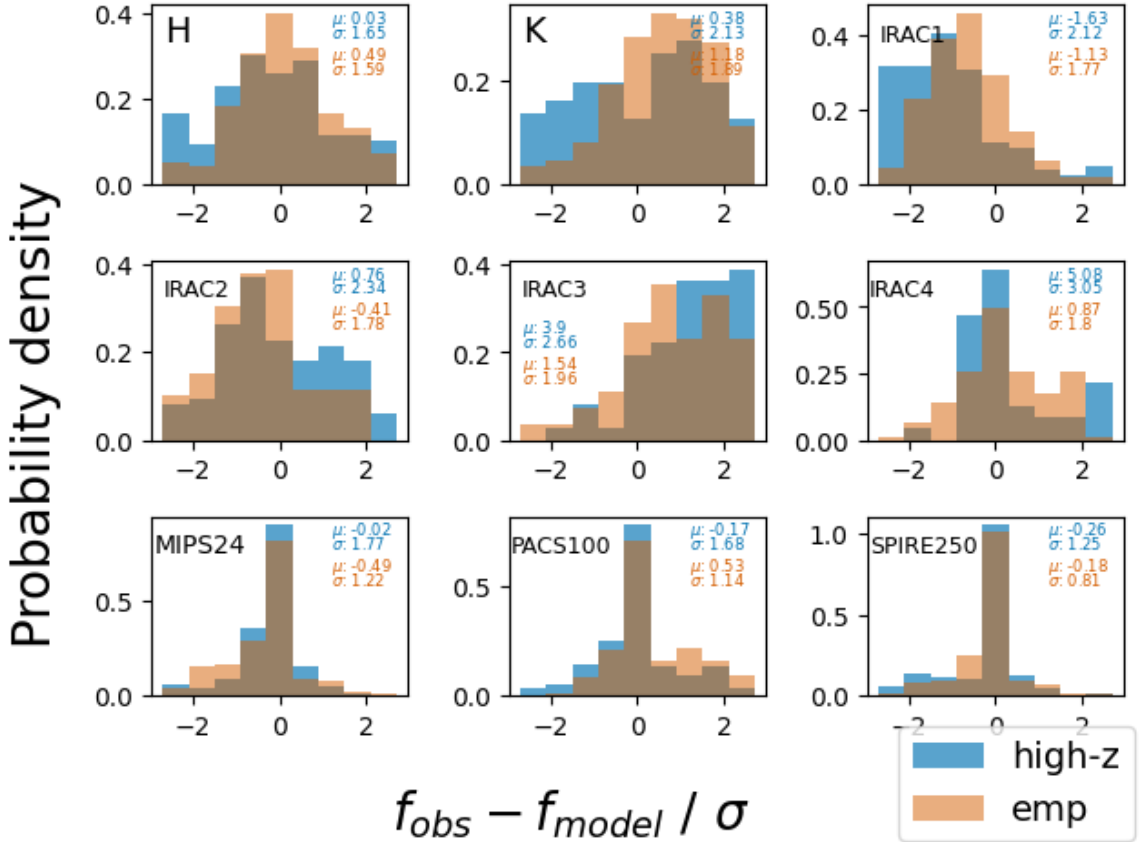


Figure 3.4: Band residual distribution for 9 different bands that were used in the SED fitting for both `highz` (brown) and AGN `emp` (blue) for the IRAC + *Spitzer/Herschel* AGN samples. We show mostly the IR bands since we focus on modelling the AGN component in the IR part and showing the residuals for seventeen other bands seems insignificant. The AGN component improves the residuals significantly for K, IRAC2, IRAC4, and MIPS24 bands and slightly well for FUV, IRAC3, PACS100, and SPIRE250 bands. However, the IRAC1 band seems to be dragged towards the positive side with the AGN component.

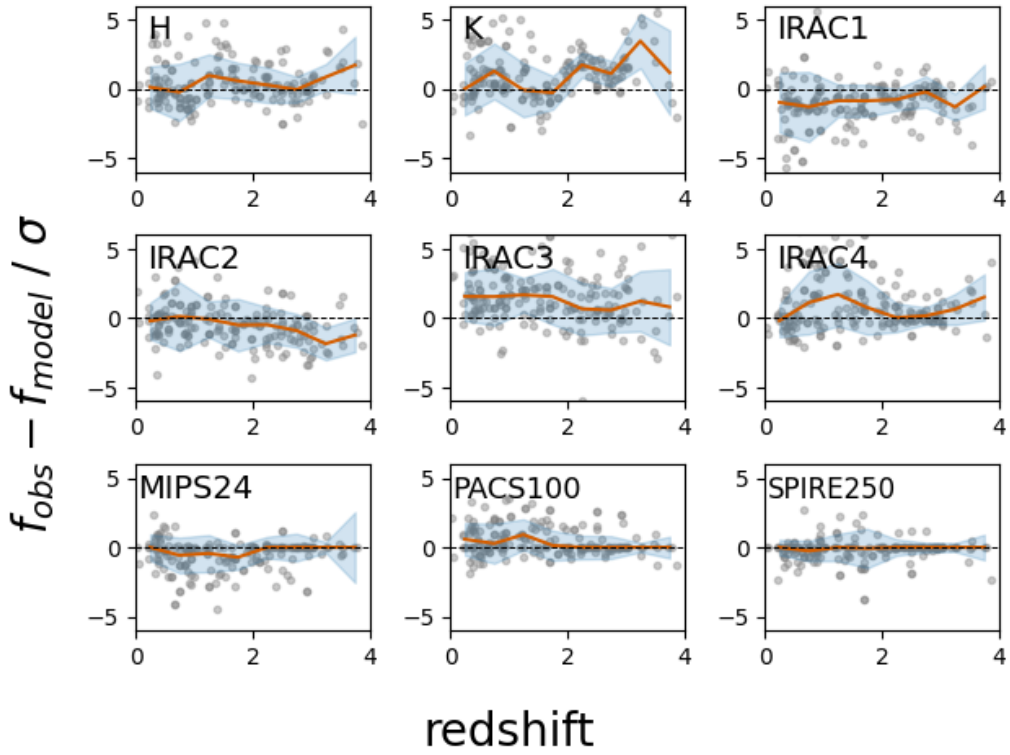
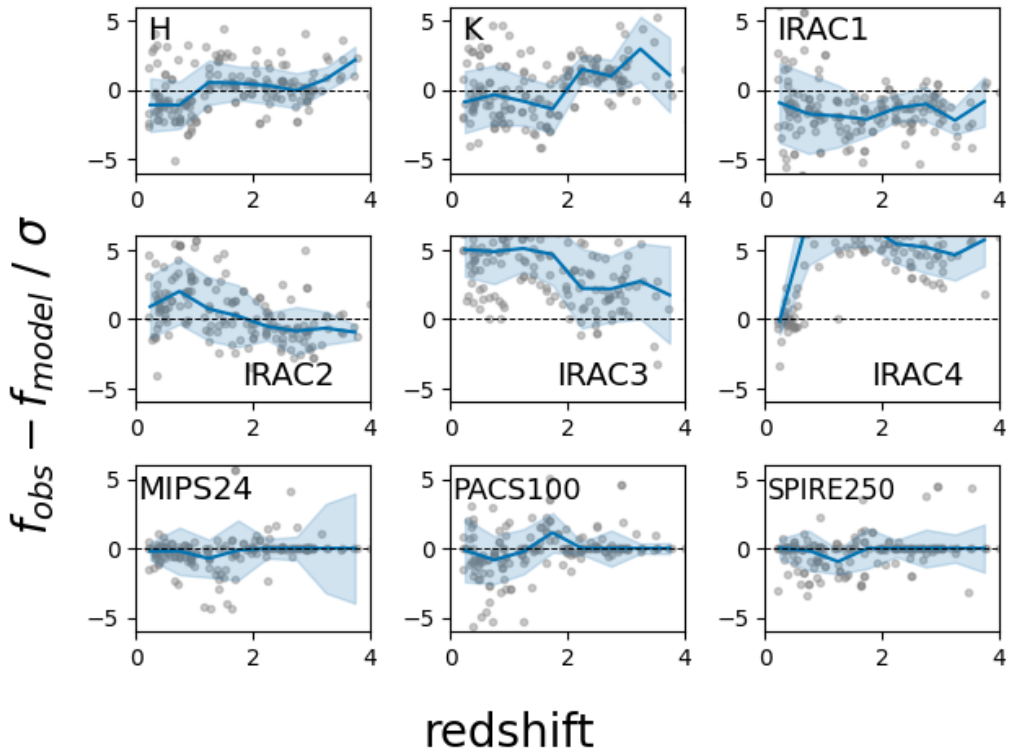


Figure 3.5: Residual evolving with redshift for the combined IR selected AGN samples. The top panel shows the residual for `highz`, bottom for `AGN emp`. The solid line is the median and the shaded portion is the standard deviation of the residuals. The dotted is the $y=0$ line. Significant improvement in the residuals seen for IRAC4 band at $z \approx 1.5$, and for MIPS24 band at $z > 1.5$

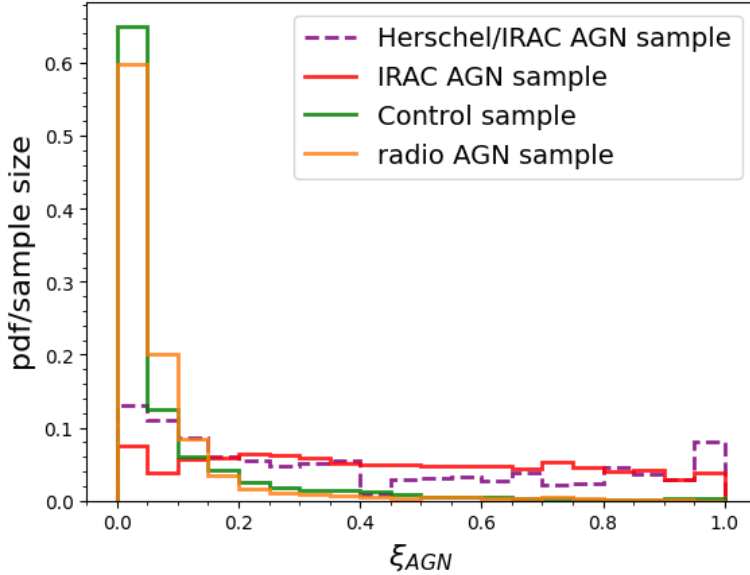


Figure 3.6: normalized PDF of ξ_{AGN} calculated by `AGN.emp` for galaxies in the 3 AGN samples and the control sample. Both IR samples show AGN fractions ranging from 0 to 1 and are spread across, whereas ξ_{AGN} peaks at zero for radio-sample galaxies and the control sample galaxies.

of all galaxies in the IRAC AGN sample and *Spitzer/Herschel* AGN sample are summed and normalized (Figure 3.6). This gives a picture of how the ξ_{AGN} is distributed for the AGN samples. We see that the PDF is mostly spread across the entire range of ξ_{AGN} from 0 to 1 for the IR AGN samples. Overall, the fraction does not seem to prefer any range and is distributed equally likely. We also note that this is for the entire sample, individual sources show preferred values of ξ_{AGN} , and the mean error of ξ_{AGN} for the IR sample galaxies is calculated (Table 3.1). We expect the distribution of ξ_{AGN} to be across the entire range since these galaxies are potential AGN candidates selected by color cut, and there would be galaxies with varying AGN contributions. We also see a high fraction of low ξ_{AGN} value. This may be due to two reasons. There might be star-forming galaxy contamination in the AGN sample. The redshift dependence of this was looked into and found that the low ξ_{AGN} was especially prevalent for the redshift range 0.2-0.8.

Another reason for the low ξ_{AGN} is due to the template selection, or the type of AGN. ξ_{AGN} is defined in the IR luminosity, while Seyfert 1 and QSO galaxies may not be dominant in IR. The next important result is the ξ_{AGN} peaked at 0 for radio AGN sample galaxies. The radio-loudness is caused by the synchrotron emission in galaxies, but the templates defined in `AGN.emp` are dominant in IR and identify AGN using their IR spectral features. So, the radio-selected AGN does not appear to be AGN prominent in mid-IR AGN template SED fitting. This is a selection bias and highlights the importance of adding a radio component in SED fitting to characterize the radio-selected AGN. We note that for the SED fitting of the radio AGN sample galaxies we added the 10GHz and 20GHz radio bands, which can affect the SED-fitting results which are even reflected in the χ^2_{red} (Figure 3.3) because of the non-availability of radio excess template for both versions of MAGPHYS. The code use SF correlation with IR, while the

excess radio flux would alter the results so that the fitting results may not be robust for this sample and hence we do not add the radio AGN sample in our further analyses.

For the control sample, the PDF of ξ_{AGN} peaks at 0. This is consistent with what we expect, as these galaxies are supposed to have low AGN components and shows that `AGN emp` can be used to effectively do the fitting of non-AGN galaxies. However, there are still galaxies in the control sample having considerable (> 0.2) ξ_{AGN} , may be those galaxies missed in the AGN space of the IR color-color space. There can be AGN outside the AGN space in the color-color space (Donley et al., 2012; Kirkpatrick et al., 2013).

Next we see that the low-redshift galaxies in the AGN sample with low ξ_{AGN} distribution, but high-redshift galaxies with high ξ_{AGN} in IR AGN samples. This is probably a result of Malmquist bias (Malmquist, 1922), which refers to the tendency to preferentially detect intrinsically bright objects. Consequently, only AGN with higher intrinsic luminosity (typically with higher ξ_{AGN}) are likely to be observed at the highest redshifts.

3.1.4 Template selection

Next, we look into how the templates are selected for each galaxy sample, each template represents a certain type of AGN in `AGN emp`. `AGN emp` gives a best-fitting template, along with the PDF of the templates selected for each galaxy. Summing up the PDF of templates for a sample can give insights into the overall template selection of the whole sample. It needs to be checked if any certain templates are preferred. For this, we considered only galaxies with at least 10% AGN contribution in the IR ($\xi_{AGN} > 0.1$). Fig 3.7 shows the normalized PDF of the templates for both IR AGN samples. For the IR-selected AGN samples, we see significant bias for Seyfert 2 galaxies. Seyfert 2 galaxies are characterized by the dust torus blocking the accretion disk, emitting characteristic spectra in the IR. Since both the samples are IR-selected, this result agrees with what we expect and is seen as selection bias resulting from our IR emission selection criteria.

3.2 Parameter Comparison

Next, we consider how the various physical parameters derived using `highz` vary when SED fitting is done using `AGN emp`. One of the main goals of implementing an AGN component in the SED fitting model is to consistently derive the physical parameters even if there is an AGN component that heats and causes dust emission. For the estimation of how the parameter comparison behaves, stellar emission parameters like M_* , SFR, sSFR, dust parameters like L_{dust}^{total} , A_V , M_{dust} and T_{dust} are analyzed here. For that, we plot each of these parameters derived using `highz` vs `AGN emp` for the AGN samples and control samples. This can give an idea of how much they correlate and how much they deviate.

To quantify the errors of the parameters derived from the `highz` and `AGN emp` models, the error for each parameter was calculated by the average of the 84th–50th percentile difference

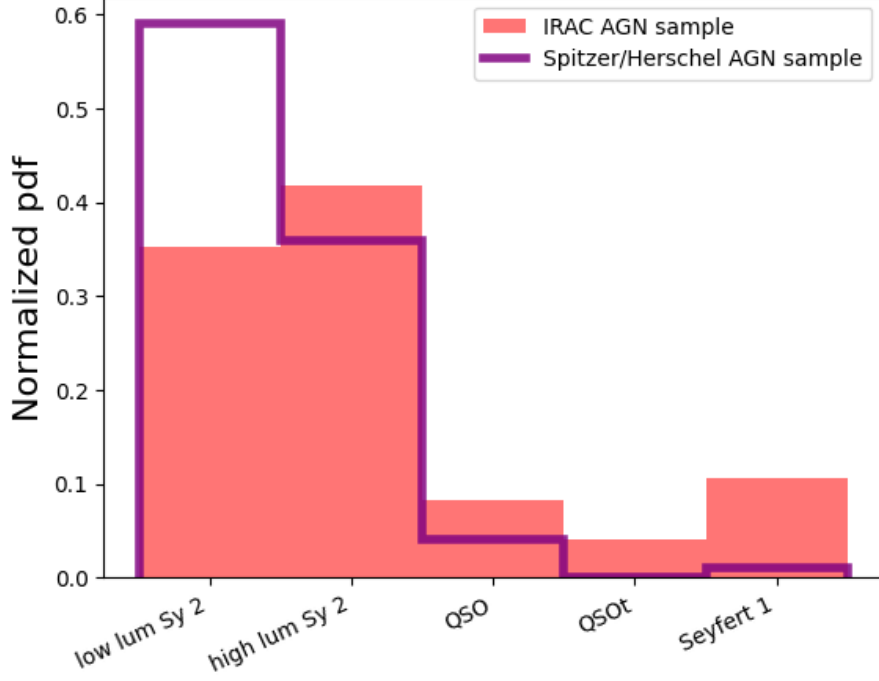


Figure 3.7: PDF of the template selection for the AGN samples, normalized by the sample size.

and the 50th–16th percentile difference of each galaxy:

$$\text{Error} = \frac{(84^{\text{th}} - 16^{\text{th}})}{2}$$

Then the mean of these errors across the entire sample computed to obtain a representative error for each parameter.

Parameter	M^* (dex)	SFR (dex)	SSFR (dex)	$L_{\text{dust}}^{\text{total}}$ (dex)	ξ_{AGN}
highz	0.0197	0.0279	0.0393	0.0389	—
AGN emp	0.0848	0.1302	0.1583	0.0949	0.0998

Table 3.1: Mean errors of the derived parameters for highz and AGN emp.

3.2.1 AGN sample

From the parameter comparison (Figure 3.8) firstly, the parameters seem to scatter for most of the galaxies considerably. The lower estimation of SFR and sSFR with an AGN component is seen in Figure 3.8a and Figure 3.8c. The contribution of AGN to the IR luminosity is separated, which results in a reduced contribution of IR emission from star formation and therefore a lower SFR estimate. This will indeed be reflected in the SFR value. However, the M_* parameter derived does not show much deviation (see Figure 3.8b), compared to the other parameters. This is because the estimation of stellar mass primarily relies on the optical and near-IR (NIR) part of the SED, where the light is dominated by old, evolved stars that contribute significantly to the galaxy’s overall luminosity for dust-obscured AGN where these wavelengths are less affected

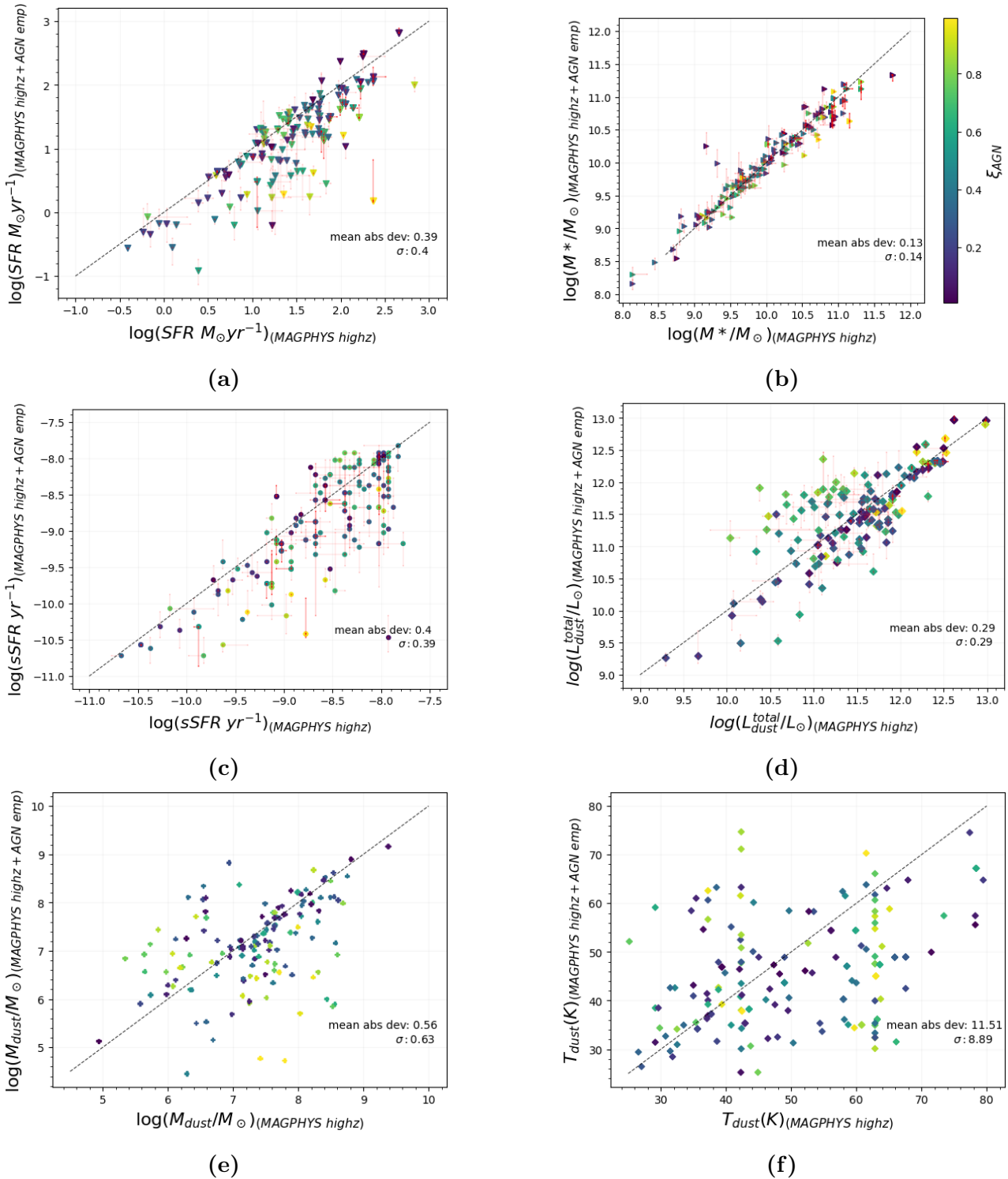


Figure 3.8: Galaxy and dust parameters comparison of AGN sample galaxies when fitted using `highz` vs `AGN.emp`. The values used here are 50th percentile from the PDF. The red bars are the error bars calculated from the 84th and 16th percentiles derived by the codes. The color gradient indicates the median value of ξ_{AGN} (50th percentile value) and is the same for all panels. For M_{dust} and T_{dust} , the best-fitting value is taken.

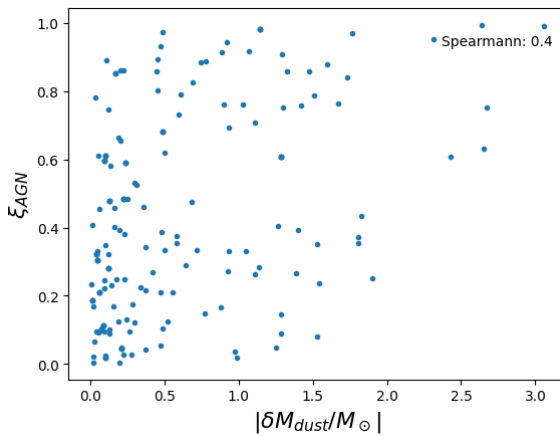
by AGN contamination compared to the mid-IR (MIR) and far-IR (FIR) regions. Another reason is that the stellar mass is derived using well-established stellar population synthesis (SPS) models, which fit the stellar light using libraries of stellar evolution tracks. These models have been refined over time and are typically robust in predicting the mass-to-light ratio (M/L) in

the optical and NIR when the emission is primarily from stars. Since dust-obscured AGN not significantly affect the M/L ratio in these bands, the stellar mass estimates remain consistent even when an AGN is present. We also see that most of the galaxies with considerable AGN fractions chose the Seyfert 2 templates, which are strong in the IR regime. This leaves the optical/UV much unaffected. The low scatter in M_* is attributed to the IR-based selection of AGN in our study. If we had selected an optical selection method, the AGN component can dominate in the optical region for the unobscured AGN, and cause larger deviation in the derived stellar mass.

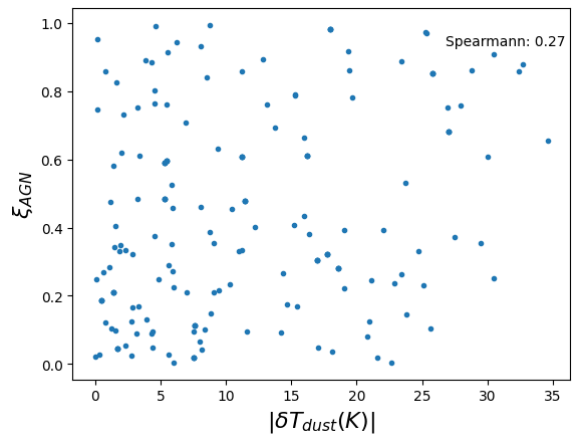
The most scatter in the parameters is seen for the dust parameters rather than the stellar emission parameters. It is the T_{dust} , M_{dust} , L_{dust}^{total} that vary the most. This happens when different IR emission models are preferred after decomposing the AGN contribution from the total dust emission at IR. The high scatter in the M_{dust} and T_{dust} (see Figure 3.8e, 3.8f) estimation shows the difficulty in disentangling the contribution of star-formation-heated dust and AGN-heated dust results in uncertainty and scatter in dust mass estimates. When the AGN component is separated, degeneracy is seen in the estimation of these two parameters. The effective temperature in a galaxy is mostly affected by the warm and hot dust grains which peak at MIR and the peak of IR whereas the dust mass is constrained by the cold dust in the galaxy peaked at the far-IR wavelength. By the removal of the AGN component in the IR, the relatively higher scatter in the derived T_{dust} than M_{dust} can be explained by this. Another reason for the degeneracy of M_{dust} and T_{dust} is the limited availability of IR data sampling the far-IR dust peak and sub-mm region that constrain these parameters (e.g., [Casey et al., 2014](#)) in our sample. Most of the galaxies do not have enough IR photometry, compared to the optical, NIR and mid-IR photometry. The sparse sampling is equally the reason for the scatter seen in the plots.

We also see from Figure 3.8 that the largest offset for most of the parameters is for galaxies with high AGN fraction (color-coded by ξ_{AGN} value in Figure 3.8). High AGN fraction galaxies are the ones that show the most deviation in derived parameters. The low AGN fraction galaxies have similar parameters between the different versions of the code. However, we also see a few galaxies with low AGN fractions having a high deviation in the derived parameters. This is because all the galaxies in the AGN sample are added in the plot, without considering the $\chi^2_{reduced}$ value. These are bad fitting results, fitted using either `highz` or `AGN emp`. The bad fits happen due to inadequate models, or bad observed data in some bands. There might be some other physical mechanism that happens in a galaxy that might not be explained in the modelling in the model SEDs.

It can be seen that the average error increased for parameters in the IR AGN sample galaxies (see Table 3.1) while fitting with `AGN emp` compared to `highz`. The introduction of more models leads to broader posterior distributions, reflecting greater uncertainty. Moreover, correlations between parameters (e.g., stellar parameters and AGN contribution) further contribute to the increased error by introducing additional variance in the fits, since a high error was seen ($\sim 10\%$) for the ξ_{AGN} parameter.



(a) Correlation plot for M_{dust} vs ξ_{AGN} .



(b) Correlation plot for T_{dust} vs ξ_{AGN} .

Figure 3.9: Overall caption for both figures.

We calculated the Spearman correlation between ξ_{AGN} and the absolute difference in the parameters calculated using `highz` and `AGN emp`. M_{dust} shows a moderate correlation of 0.40 (Figure 3.9), while other parameters show only a weak correlation (< 0.35). Comparing the correlation between M_{dust} and T_{dust} , we expect the latter to be more correlated to AGN fraction than the former as dust mass is contained by the far-IR part of the spectrum while the effective dust temperature is constrained by the warm grain emission. However, the result suggest the degeneracy of M_{dust} due to the unavailability of photometry in the far-IR part for most galaxies.

3.2.2 Control Sample

Now we compare the parameters derived using `highz` and `AGN emp` for the control sample galaxies.

The parameters do not seem to deviate but agree with each other for the control sample galaxies when fitted with `highz` and `AGN emp`. Since we assume the majority of the galaxies in the Control sample to be non-AGN, the results appear to agree with expectation. As we saw the distribution of ξ_{AGN} peaks at zero, `AGN emp` can be used to fit AGN-hosting and non-AGN galaxies (even though with longer computational time). However, a few galaxies in the Control sample have high ξ_{AGN} values, indicating they may be AGN that escaped the selection process and the color-color space used.

3.3 Limitations of AGN emp

We can see in Figure 3.8 that there are a lot of outliers in the AGN-sampled galaxies with large χ^2 values. We cannot interpret the physical parameters derived from a galaxy with a high χ^2 value nor interpret the SED because it is likely that the models are not representative of the observations for these cases. This happens because of the low flexibility of data, or insufficient modelling in the SED fitting. There are also galaxies with high spread in the derived galaxy and dust parameters. The high error in ξ_{AGN} parameter, poorly constrained

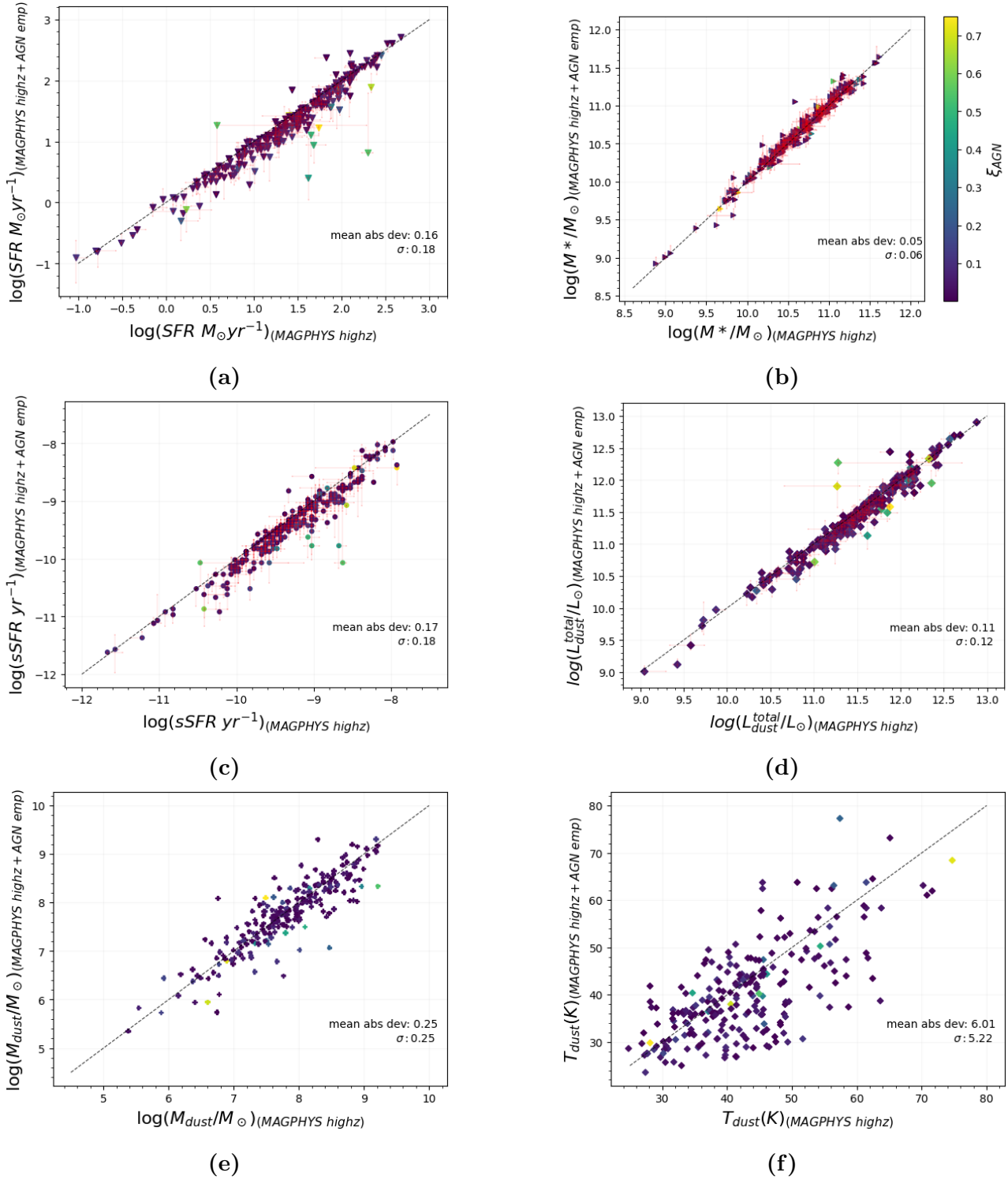


Figure 3.10: Parameters comparison of AGN sample galaxies when fitted using `highz` vs `AGN.emp`. The values used here are 50th percentile from the PDF. The red bars are the error bars. The color gradient is for varying values of ξ_{AGN} (50th percentile value). For M_{dust} and T_{dust} , the best-fitting value is taken.

parameters are also not reliable. To explain the IR-selected AGN candidate galaxies, we may need more models in the SED fitting code. Dust heating by the AGN and emission in the IR can be modelled flexibly if there are more dust emission models added to it. Seyfert 2 AGN are cases where the accretion disk is obscured by dust and causes IR emission. In the `AGN.emp`

version we have only 2 templates for Seyfert 2 galaxies. We also see that AGN sample galaxies with $\xi_{AGN} \geq 0.1$ prefer Seyfert 2 galaxy templates over the other templates. Adding more templates to the AGN version of **MAGPHYS** may reduce the number of outliers.

Empirical AGN templates are derived by combining observed data. They are limited by observational bias and can miss the diversity of AGN properties. We see that the stellar emission and dust emission are modelled in a physically motivated way, and these are compared to the observed data to constrain different properties. However, in contrast to the empirical templates, AGN can also be modelled in a physically motivated manner, relying on radiative transfer simulations that capture key processes like dust absorption, scattering, and re-emission of a dust torus around a central supermassive black hole. These models align with the AGN unification model, using parameters such as inclination and opening angles to explain both obscured and unobscured AGN. Unlike static templates, torus models are adaptable to new data and better handle degeneracy in SED fitting, offering improved predictive power for identifying AGN across different environments, including high-redshift sources. We explore the torus emission SED created by [Stalevski et al. \(2012\)](#) for a 2-phased torus model for a varying viewing angle and dust density parameters, in the next chapter. We explore how they can be incorporated into **MAGPHYS+AGN**, and how they can affect the SED fitting process.

Chapter 4

AGN Torus Model

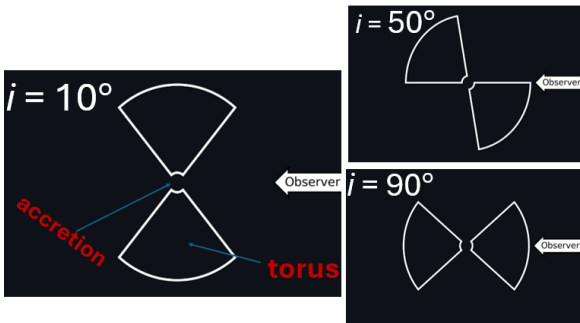
As already mentioned in the previous sections, the Unified Model of AGN favours modelling the central accretion disk of a supermassive black hole surrounded by dust as a toroidal structure (Urry & Padovani, 1995; Antonucci, 1993). Stalevski et al. (2012) modelled the dusty tori as a two-phase medium, with high-density dust clumps and low-density medium filling the space between the clumps. The dust contains separate populations of graphite and silicate grains. They modelled the SEDs of the torus model for a grid of parameters using the open source code SKIRT (Baes et al., 2011) which is a 3-D Monte Carlo radiative transfer code for simulating continuum radiation transfer in dusty astrophysical systems. The SED models are publicly available¹, and there is a combination of SEDs for different values of parameters which totals 19,200 SEDs for the torus emission model. Below we summarise the parameters and their physical meaning, and how the SED changes for each parameter by keeping the others constant.

The primary source of dust heating adopted by Stalevski et al. (2012) is the intense UV/optical continuum emitted isotropically from the supermassive black hole accretion disc modelled as a point-like energy source. Its SED is approximated by a series of power laws across different wavelength ranges, with values derived from both observational and theoretical studies, demonstrating minimal impact on IR re-emission from changes in the SED shape.

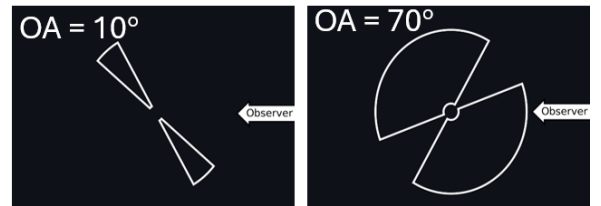
The range of values of the torus parameters are given in Table 4.1. For the grid of varying parameters, the first parameter is the viewing angle of the accretion disk, which determines if the accretion disk is viewed directly or if the torus is in between the central black hole and the observer. The viewing angle is defined in terms of the inclination angle (i) to the line of sight and the opening angle of the torus. $i = 0$ degrees corresponds to the face-on view where the observer sees the accretion disc directly, while an $i = 90$ degrees is the edge-on view where the accretion disc is completely obscured by the torus (Figure 4.1a).

Next, the opening angle (OA) of the torus is a measure of the angular extent of the torus around the central black hole. It defines the boundary between a region obscured by the torus and a directly visible region. A low half-opening angle would cover less region of the spherical sky around the accretion disk, while a higher angle suggests more region covered by the torus (Figure 4.1b). The viewing angle would be a combination of the opening angle and inclination

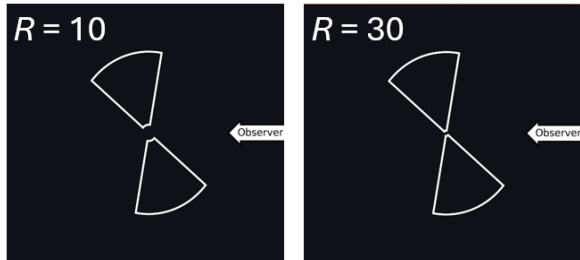
¹For more information, visit <https://sites.google.com/site/skirtorus/home>.



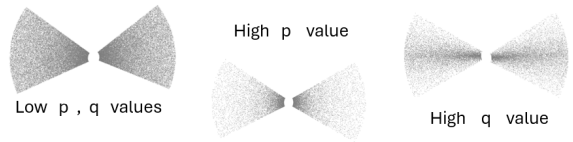
(a) varying inclination angle of the torus.



(b) Varying opening angle of torus



(c) Low and high outer radius/inner radius ratio



(d) Varying dust density parameters. the second image is for a high radial density gradient index, third image is for a higher angular density gradient index.

Figure 4.1: 2-D representation of how the viewing angle and density parameters change. The cones are a cross-section of the dust torus around the AGN. Figures in a,b, and c are taken from <https://skirtor.streamlit.app/>

angle, as i and OA increase the amount of obscuration also increases.

The next parameter is the ratio of the outer radius (R_{out}) to the inner radius (R_{in}) of the torus (R). R_{in} is set to 0.5 pc, and SEDs for different values of R are given. A higher value of R implies a larger torus structure (Figure 4.1c). The density of the torus is described by the index of radial density gradient (p) and index for angular density gradient (q) (Figure 4.1d). The spatial density of dust is described by

$$\rho(r, \theta) \propto r^{-p} e^{-q|\cos(\theta)|} \quad (4.1)$$

where p controls how dust density changes with the distance from the centre of the torus (r) and q controls how dust density varies with the angle above or below the equatorial plane of the torus. A higher value of p implies a steeper drop in density outward from the centre, meaning the dust is more concentrated towards the inner regions of the torus. A higher q means the dust density decreases more rapidly as you move away from the equator toward the poles of the torus. This helps shape the vertical structure of the dust distribution, influencing whether the torus is more puffed up or flattened.

The next parameter is the average edge-on optical depth at 9.7 μm ($\tau_{9.7}$), which measures how opaque the torus is to radiation at that wavelength. A higher value of $\tau_{9.7}$ means the torus absorbs more radiation at 9.7 μm , which corresponds to silicate dust features. High values of $\tau_{9.7}$ mean a high column density of silicates in the line of sight.

Another parameter is the fraction of total dust mass inside clumps (Mcl). This is set as

0.97, implying 97 percent of the dust mass is in the clumps. There is only one value for this parameter in the SED library.

Parameter	Values
Inclination angle i (degrees)	0, 10, 20, 30, 40, 50, 60, 70, 80, 90
Opening angle (OA) (degrees)	10, 20, 30, 40, 50, 60, 70, 80
Average edge-on optical depth $\tau_{9.7}$	3, 5, 7, 9, 11
Radial density gradient index p	0, 0.5, 1, 1.5
Angular density gradient index q	0, 0.5, 1, 1.5
Outer-to-inner radius ratio R	10, 20, 30
Fraction of dust mass in clumps M_{cl}	0.97

Table 4.1: Torus model parameters and their values for the SED library in Stalevski et al. (2012).

We investigated how the different parameters affect the SED of the accretion disk emission. For that, the SED for varying values of each parameter is plotted while keeping the other parameters constant at a mid-value (4.2). The major distinguishing features are the 9.7-micron feature and the change in SED happening before 1 μm . The 9.7 μm emission arises from the silicate dust in the accretion disk that is heated to a high temperature. For dust-free lines of sight, this feature is seen in emission, which can be seen in the figure for $i = 40$ degrees and $OA = 40$ degrees. But when the torus obscures the dust, the emission feature is scattered, while giving an absorption feature at 9.7 μm by the silicate grains present in the torus. The next important feature is the continuum before 1 μm . The dust-free line of sight allows the accretion disk emission seen emission, but it is scattered by the dust in the torus for higher inclination and opening angles. The greatest difference in the SED is seen for varying OA , more area of dust covering the accretion disk will make it scatter the accretion disk continuum. The changing radius ratio can also affect the SED in scattering the continuum. A low ratio means that the accretion disk is not tightly bound by the torus, and the scatter is lower compared to the higher radius ratio.

Varying values of p , q , and $\tau_{9.7}$ can also have an impact on the SED of the torus emission. Dust distributed all across the torus consistently (low q) can cause more scatter than the density steeply decreasing from the equatorial plane to the poles (high value of q). The absorption feature of 9.7 μm is also deep for the lowest value of q . Compared to other parameters, the optical depth and radial density index parameters have less impact on the SED. However, they also impact on the SED. For very low values of $\tau_{9.7}$, the column density of dust that absorbs the 9.7-micron wavelength is low, and the silicate emission is seen in emission even through the obscuring torus.

4.1 Addition of Torus templates

For the grid of 6 parameters that are described above, a total of 19200 SED for the Stalevski torus emission model available are added to the MAGPHYS+AGN version of the code to investigate

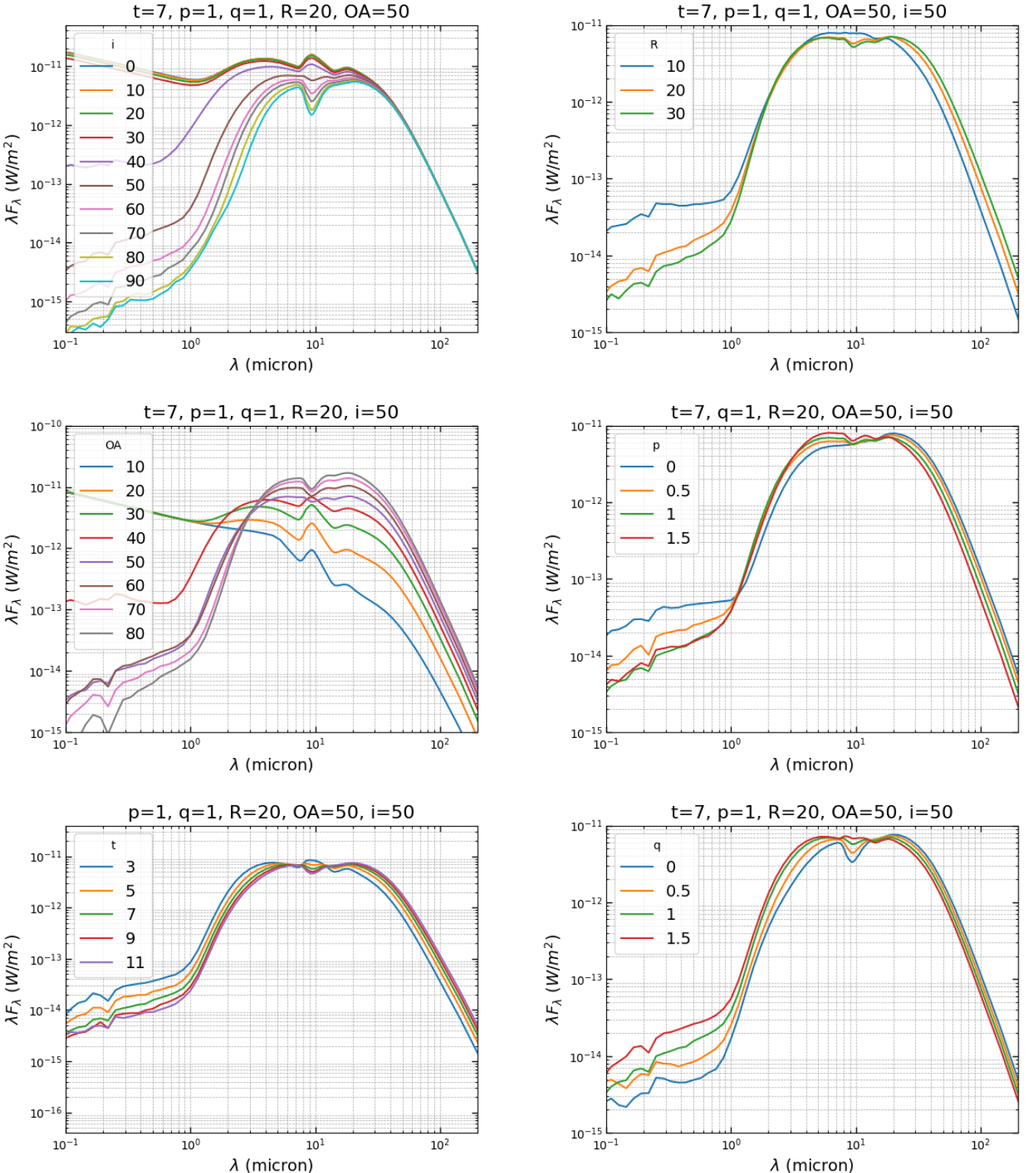


Figure 4.2: Demonstration of how the Stalevski(2012) SEDs change for varying parameters, keeping the other parameters constant. For the constant other parameters, the mid value is taken. The SEDs plotted are total SEDs which is the sum AGN+torus+scattered. The main features are at $1\mu\text{m}$ and $9.7\mu\text{m}$, depending on the viewing angle of the torus.

how they would impact the total SED fitting. This allows greater flexibility to accurately model the variety of SEDs observed, accounting for the differences in dust content, distribution, and viewing angle, enabling the fitting to reflect the diversity in AGN environments. This approach also improves the characterization of both obscured and unobscured AGNs and enhances the ability to capture anisotropic emission patterns that vary with orientation. The whole SED library was added to the `MAGPHYS+AGN` version, this version is mentioned as ‘`MAGPHYS+AGN torus`’ or simply ‘`AGN torus`’, from now on. Another reason for adding all the templates is to understand how well the various parameters can be constrained. We edited the fitting code such that the fitting process will give the PDF and best-fitting values of the 6 torus parameters in the [Stalevski et al. \(2012\)](#) model. This allows us to study the various torus parameters of the observed SED of galaxies. We will also test using subsets of the templates which will allow the code to run much faster. The ultimate goal is to find a good balance between the accuracy of derived parameters and computational efficiency.

The SED fitting for a sub-sample of galaxies in the IRAC AGN sample was done with this version. The computation time for running the code is high (for the `AGN emp` version it is just minutes but for `AGN torus` version it is hours, as the number of models is multiplied by thousands). Therefore a ‘`reduced torus`’ version is made, where only 2400 of the 19200 templates will be run. This is done by random sampling of the torus templates, in the main fitting code. However, we need to ensure that the parameter space is well-sampled for this version of the code. To investigate that, we run the SED fitting using both the full and reduced version of the ‘`AGN torus`’ model for a subset of galaxies in the IRAC AGN sample. From the results of the two versions of the ‘`AGN torus`’ code, the torus parameters are compared ([4.3](#)) to see how well the parameter space is sampled for each version.

We find that the torus parameters derived using the reduced AGN torus template set show minimal deviation from those obtained with the full template set ([Figure 4.3b](#)). Both versions effectively explore similar regions of the parameter space ([Figure 4.3a](#)), ensuring that the results remain consistent. Additionally, the χ^2 statistic for a representative sub-sample remains almost unchanged ([Figure 4.3c](#)), indicating that the reduced template version provides a comparable quality of fit. The comparison of error for individual galaxies for the ξ_{AGN} also does not vary much ([Figure 4.3d](#)).

Using the reduced template set offers a practical advantage—it significantly reduces computation time without compromising the accuracy or reliability of the SED fitting. This makes the code more efficient, especially for large datasets, while still capturing the essential dust geometry and orientation effects modelled by the torus parameters. Therefore, we safely adopt the reduced AGN torus template version for SED fitting in subsequent analyses.

4.2 Testing AGN torus on a robust AGN sample

[Kirkpatrick et al. \(2012\)](#) decomposed the mid-IR spectrum of 151 galaxies in the GOODS-N and ECDFS fields having *Spitzer* IRS spectroscopy selected at $S_{24\mu m}$, into star-forming and AGN

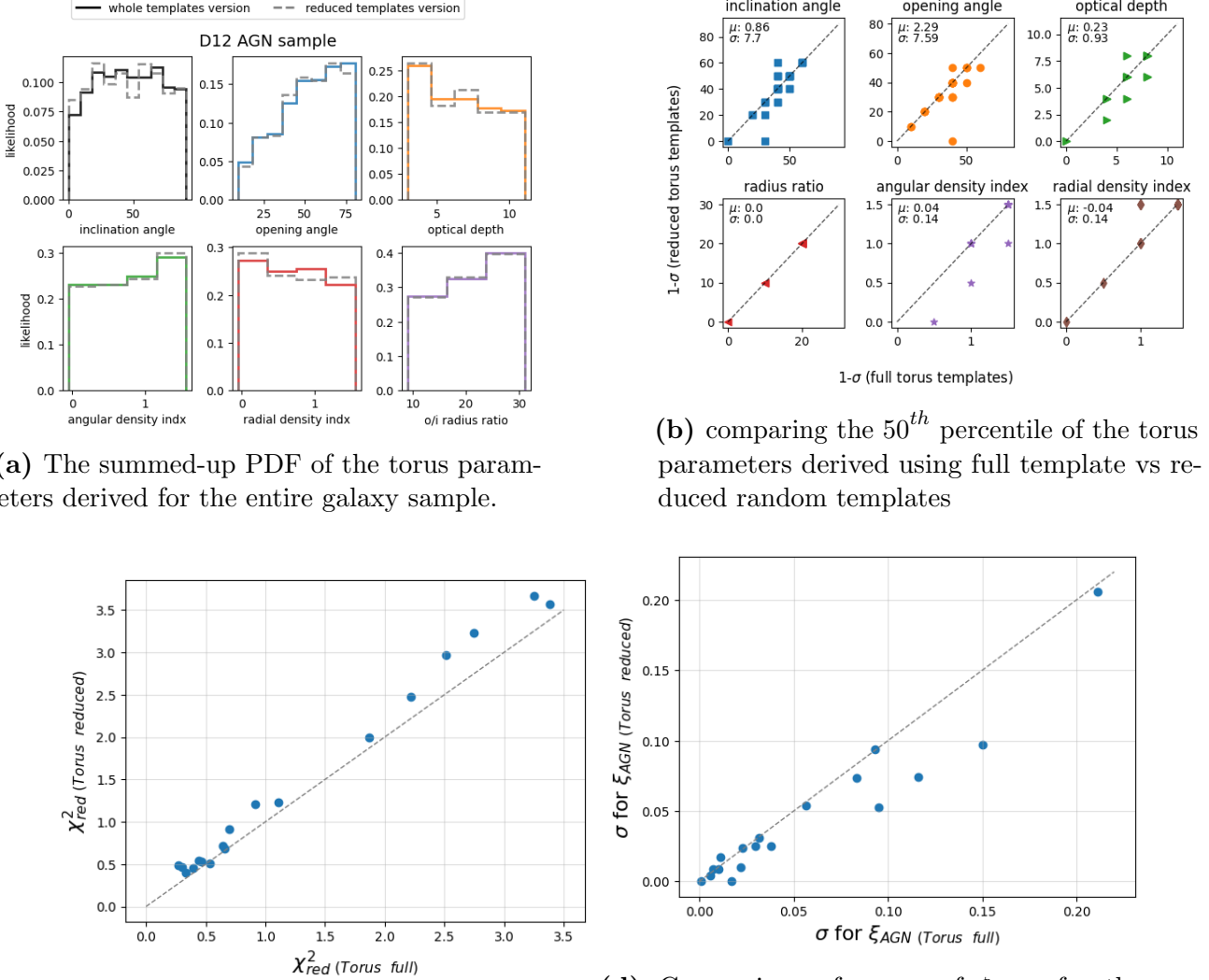


Figure 4.3: Comparing the ‘full’ vs ‘reduced’ AGN torus version of MAGPHYS+AGN.

components. Then they computed the relative strength of AGN in the IR (8-1000 μm) and classified the galaxies into star-forming, featureless AGN, and silicate AGN galaxy categories (Figure 4.4b). The photometry for the IR for these galaxies is given in the paper ($S_{24\mu\text{m}}$, $S_{70\mu\text{m}}$, $S_{100\mu\text{m}}$, $S_{160\mu\text{m}}$, $S_{250\mu\text{m}}$, $S_{350\mu\text{m}}$, $S_{500\mu\text{m}}$). We compared the AGN strength of these galaxies calculated by Kirkpatrick et al. (2012) to the ξ_{AGN} value calculated by AGN torus.

For this, we matched these galaxies with the photometry for UV to mid-IR from the GOODS-N catalogue (Barro et al., 2019). We selected a sub-sample of 18 galaxies ensuring representation of varying AGN fractions calculated by Kirkpatrick et al. (2012). Then the SED fitting was done using the AGN torus version to obtain the ξ_{AGN} value. The ξ_{AGN} values derived from our AGN torus model show good agreement (see Figure 4.4a) with the AGN fraction reported by Kirkpatrick et al. (2012), which is considered a reliable, spectroscopically derived measure. While the wavelength ranges differ—our model covers 3-1000 μm and Kirkpatrick’s analysis focuses on 8-1000 μm —the overlap in the mid-IR ensures both methods capture the core AGN emission. We also calculated the AGN fraction from the best-fitting SED for 8-1000 μm but it does not seem to agree with the Kirkpatrick et al. (2012) values for the 3 featureless AGN. The value derived from best-fitting SED may not be robust. However, the silicate AGN appears to be almost agreeing with the AGN fraction values. The median ξ_{AGN} values almost agrees with the agn fraction from Kirkpatrick et al. (2012).

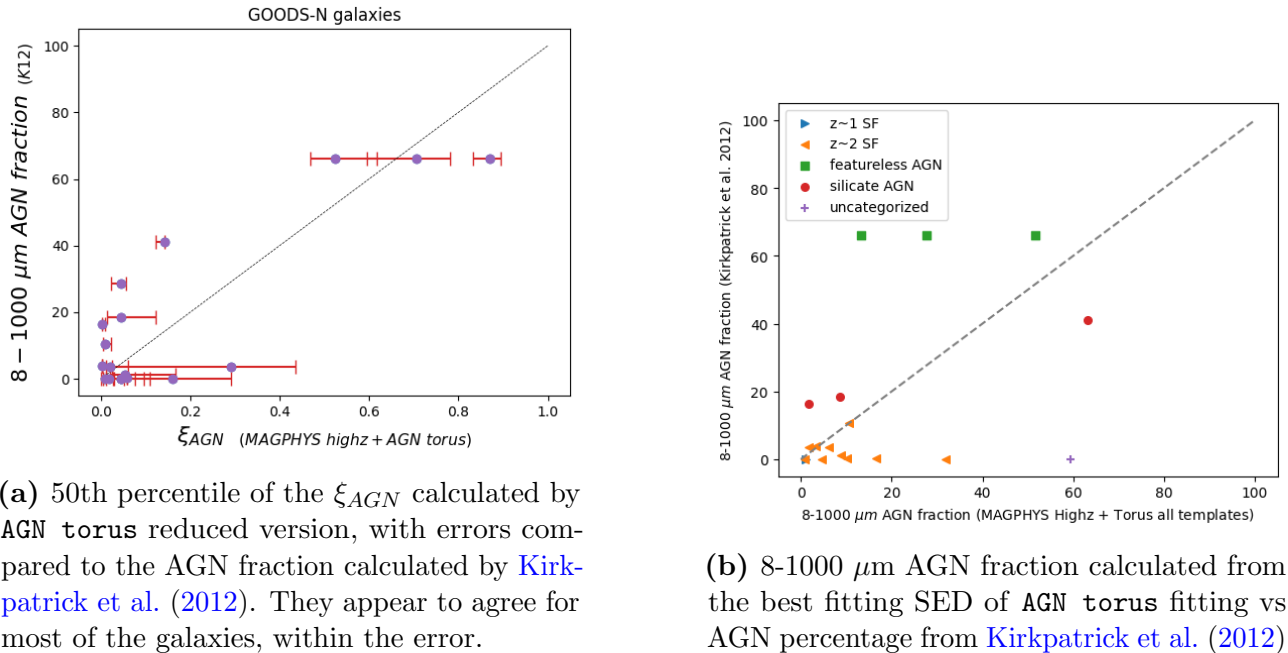


Figure 4.4: AGN percentage comparison

4.3 Summary

We integrated the torus templates and worked to constrain the associated parameters. Further testing and optimization are required, utilizing samples with accurately calculated AGN fractions and high-quality, reliable photometry.

Chapter 5

Discussion and Conclusion

5.1 Discussion and Conclusion

In many astrophysical studies, AGN-contaminated galaxies are often removed from sample datasets to simplify analysis. However, this approach can lead to a significant loss of valuable information, as it ignores the interplay between star formation and AGN activity in galaxy evolution. By incorporating an AGN component into SED fitting codes, we can effectively model the contributions of both star formation and AGN activity to the total observed flux. Integrating an AGN component helps solve the biases introduced by simply excluding AGN-dominated sources. It ultimately enhances the comprehensiveness of studies involving galaxy populations, particularly in high-redshift environments where AGN activity is prevalent.

We attempted to constrain the torus parameters of the AGN component through SED fitting although we find these parameters are not constrained well with current photometric data. This is especially useful for galaxies with or without AGN components at high redshifts. This torus templates version is consistent with the unification model, rather than the empirically derived templates fitting. However, there needs to be further improvements in the template addition, which will be discussed here.

To rephrase from [da Cunha et al. \(2008\)](#), MAGPHYS is a “simple, largely empirical but physically motivated model to interpret the mid- and far-IR SEDs of galaxies consistently with the emission at UV, optical and near-IR wavelengths”. How MAGPHYS stands out from other SED fitting models is its easy-to-use, physically motivated nature and low computational resource usage. For characterising the AGN SED in a physically motivated way, we replaced the empirical templates with the torus emission templates ([Stalevski et al., 2012](#)), the two-phased torus model being modelled according to the unification model, and having a realistic torus dust distribution than the clumps only and smooth dust distribution ([Wada, 2015](#)).

However, the computation time was very high when 19200 templates were added to the fitting code. We might not need the high computation time for fitting the SED of a single galaxy to constrain the torus parameters by the vast number of models. This can be resolved in the future by reducing the parameter space. For instance, taking only the extreme values of the radial dust density gradient ensures coverage of both simple and complex density distributions.

The opening angle-inclination angle degeneracy also needed to be taken into account. Similarly, reducing the other torus parameters' space considerably reduces the number of tori AGN and the computation time.

We found the low ξ_{AGN} for some of the galaxies in the AGN sample in our results. This can be explained by the contamination of star-forming galaxies in the AGN space, as these IR selections are not 100 percent accurate. There might also be errors for high redshift galaxies for the IR photometry from the [Jin et al. \(2023\)](#) super-deblended catalogue. The IR data were sourced from the super-deblended photometry catalogue, which aims to resolve blended sources in crowded fields. However, the deblending process introduces uncertainties that can affect flux measurements, especially at longer wavelengths where multiple sources overlap. These uncertainties may lead to deviations in the SED fitting results, highlighting the need for careful treatment of IR photometry and the potential benefit of deeper, higher-resolution observations. Surveys like Galaxy And Mass Assembly (GAMA, [Driver et al., 2022](#)) provide deep photometry for spectroscopic redshift for a vast number of galaxies at low redshift. The SED fitting with `AGN torus` model can be done in the future for the galaxies at low redshift.

It was shown that the most different and well-studied part of the SED that shows significant comparison is the silicate feature which lies in between $10 \sim 20 \mu\text{m}$ rest-wavelength. However, we had only a few photometry points from the *Spitzer* (3.6-24 μm) and *Herschel* (70,100 μm) telescopes. The *Spitzer* MIPS 24-micron filter is the only available filter in the COSMOS and GOODS survey galaxies where the silicate feature can be directly observed but for higher redshift. With this limited number of photometry points, it would be difficult to constrain the torus parameters properly.

With the unprecedented sensitivity and resolution of JWST/MIRI from upcoming surveys like SMILES ([Alberts et al., 2024](#)), it is now possible to detect fainter AGN at higher redshifts, providing crucial insights into the early stages of black hole and galaxy co-evolution. The mid-IR coverage will also allow us to differentiate between AGN emission and that from star-forming regions, reducing contamination in SED modelling. The detailed observation of silicate absorption and emission features at 9.7 and 18 microns will help constrain the dust composition, optical depth, and geometry of the torus. This will further refine models of the obscuring structures, offering a better understanding of AGN unification schemes.

Looking ahead, the PRIMA space telescope ([Mouillet et al., 2023](#)) will complement JWST by probing the far-IR regime, unveiling cold dust components and AGN feedback effects. With its wide wavelength coverage, PRIMA will aid the study of dust reprocessing across different environments, providing better constraints on the torus size and structure at high redshifts. These advancements will make it possible to trace SMBH growth through cosmic time, enhancing our understanding of the interplay between AGN activity and galaxy evolution.

The majority of AGN are found to be obscured by dust, as highlighted by [Hickox & Alexander \(2018\)](#). This obscuration is typically quantified by comparing the infrared (IR) luminosity with X-ray photometry, a method that allows for a clearer understanding of the AGN's intrinsic properties, particularly in cases where X-ray counterparts are available ([Laloux](#)

(et al., 2022). By examining the relationship between these two measurements, researchers can infer the level of obscuration affecting the AGN.

For galaxies with X-ray counterparts, it becomes feasible to model the obscured AGN population in a coherent manner using the torus emission parameters. The SED generated from various configurations of radial dust density distribution and optical depth offers a valuable tool for this modeling. Although this specific approach has not been tested in the current work, it presents an exciting avenue for future research. Exploring this relationship could enhance our understanding of the physical conditions surrounding obscured AGNs and their impact on galaxy evolution, ultimately contributing to a more comprehensive picture of the AGN population across different environments and epochs.

More recent torus emission models, for example, González-Martín, Omaira et al. (2023) modelled the SED for AGN tori with a 2-phased medium of dust distributed as clumps and smooth dust. They explored the changes in the SED for varying grain sizes of the dust distribution. The addition of these complex models would increase parameter space and increase the computation time. However, more realistic versions of torus emission could be explored in the future.

Other SED fitting codes include AGN components and identify AGN such as AGNfitter (Calistro Rivera et al., 2016), ProSpect (Thorne et al., 2022), GRAHSP (Buchner et al., 2024). Comparison of SED fitting code is done by some of the works in the past (e.g: Hunt, L. K. et al., 2019; Pacifici et al., 2023), to see how the different SED fitting codes can retrieve galaxy parameters. In this work, we did not do a comparison between MAGPHYS+AGN code and other SED fitting codes since this is beyond the scope of this work. Also, each SED fitting code serves a different purpose, maybe the number of parameters varies from code to code. It would be worth comparing the different SED fitting codes including AGN components and how they parameterize different aspects of AGN-hosting galaxies.

5.2 Summary

We created potential AGN candidate galaxy samples by separating them in the IR colour-colour space, along with a control sample, for galaxies with spectroscopic redshift ($0 \sim 4$) in the COSMOS2020 catalogue. SED fitting was done for all the galaxies in these samples using MAGPHYS `highz` (da Cunha et al., 2015) and MAGPHYS+AGN `emp` (Chang et al., 2017). It was found that 131/142 galaxies in the IRAC AGN sample and 30/39 galaxies in the *Spitzer/Herschel* AGN sample had $\xi_{AGN} > 0.1$ when fitted with MAGPHYS+AGN `emp`.

It was shown that including the AGN component makes the fitting code more flexible, and the mid-IR part is fitted for AGN candidate galaxies by including AGN templates in the code. The stellar and dust properties derived after separating the AGN component in galaxies deviate from the parameters derived without separating the AGN component in the SED fitting process. MAGPHYS+AGN can do the SED fitting for galaxies with or without the AGN component.

We added torus emission templates of Stalevski et al. (2012) to make the modified version

MAGPHYS+AGN torus, with viewing angle and dust density parameters of the torus. To constrain the new parameters, this latest version needs more testing using more photometric data in the MIR.

From fitting the radio-loud AGN we saw the importance of adding a radio component in the SED fitting code to characterise the radio-loud AGN, in the SED fitting code.

Bibliography

- Alberts S., et al., 2024, arXiv e-prints, p. arXiv:2405.15972
- Alexander D. M., Hickox R. C., 2012, *New Astron. Rev.*, 56, 93
- Allamandola L. J., Tielens A. G. G. M., Barker J. R., 1989, *Astrophys. J., Suppl. Ser.*, 71, 733
- Antonucci R., 1993, *Annu. Rev. Astron. Astrophys.*, 31, 473
- Antonucci R. R. J., Miller J. S., 1985, *Astrophys. J.*, 297, 621
- Arnouts S., et al., 2002, *Monthly Notices of the Royal Astronomical Society*, 329, 355
- Assef R. J., et al., 2013, *The Astrophysical Journal*, 772, 26
- Baes M., Verstappen J., Looze I. D., Fritz J., Saftly W., Pérez E. V., Stalevski M., Valcke S., 2011, *The Astrophysical Journal Supplement Series*, 196, 22
- Baldwin J. A., Phillips M. M., Terlevich R., 1981, *Publ. Astron. Soc. Pac.*, 93, 5
- Barro G., et al., 2019, *Astrophys. J., Suppl. Ser.*, 243, 22
- Battisti A. J., et al., 2019, *The Astrophysical Journal*, 882, 61
- Brammer G. B., van Dokkum P. G., Coppi P., 2008, *Astrophys. J.*, 686, 1503
- Brandt W. N., Alexander D. M., 2015, *The Astronomy and Astrophysics Review*, 23
- Brightman M., Nandra K., Salvato M., Hsu L.-T., Aird J., Rangel C., 2014, *Monthly Notices of the Royal Astronomical Society*, 443, 1999
- Bruzual G., Charlot S., 2003, *Mon. Notices Royal Astron. Soc.*, 344, 1000
- Buchner J., et al., 2015, *The Astrophysical Journal*, 802, 89
- Buchner J., et al., 2024, Genuine Retrieval of the AGN Host Stellar Population (GRAHSP) ([arXiv:2405.19297](https://arxiv.org/abs/2405.19297)), <https://arxiv.org/abs/2405.19297>
- Calistro Rivera G., Lusso E., Hennawi J. F., Hogg D. W., 2016, AGNfitter: SED-fitting code for AGN and galaxies from a MCMC approach, *Astrophysics Source Code Library*, record ascl:1607.001

- Calzetti D., Armus L., Bohlin R. C., Kinney A. L., Koornneef J., Storchi-Bergmann T., 2000, *Astrophys. J.*, 533, 682
- Capak P., et al., 2007, *The Astrophysical Journal Supplement Series*, 172, 99–116
- Casey C. M., Narayanan D., Cooray A., 2014, *Phys. Rep.*, 541, 45
- Chang Y.-Y., et al., 2017, *Astrophys. J., Suppl. Ser.*, 233, 19
- Charlot S., Fall S. M., 2000, *Astrophys. J.*, 539, 718
- Chevallard J., Charlot S., 2016, *Monthly Notices of the Royal Astronomical Society*, 462, 1415
- Chiappetti L., et al., 2005, *Astronomy and Astrophysics*, 439, 413
- Comastri A., 2004,] 10.1007/978-1-4020-2471-9₈
- Condon J. J., 1992, *Annual Review of Astronomy and Astrophysics*, 30, 575
- Conroy C., 2013, *Annual Review of Astronomy and Astrophysics*, 51, 393–455
- Delvecchio I., et al., 2017, *Astronomy & Astrophysics*, 602, A3
- Donley J. L., et al., 2012, *Astrophys. J.*, 748, 142
- Draine B., 2003, *Annual Review of Astronomy and Astrophysics*, 41, 241
- Driver S. P., et al., 2018, *Mon. Notices Royal Astron. Soc.*, 475, 2891
- Driver S. P., et al., 2022, *Monthly Notices of the Royal Astronomical Society*, 513, 439–467
- Dullemond, C. P. van Bemmel, I. M. 2005, *A&A*, 436, 47
- Feltre A., Hatziminaoglou E., Fritz J., Franceschini A., 2012, *Monthly Notices of the Royal Astronomical Society*, 426, 120
- Fritz J., Franceschini A., Hatziminaoglou E., 2006, *Monthly Notices of the Royal Astronomical Society*, 366, 767
- Galliano F., Galametz M., Jones A. P., 2018, *Annu. Rev. Astron. Astrophys.*, 56, 673
- González-Martín, Omaira et al., 2023, *A&A*, 676, A73
- Hao L., et al., 2005a, *The Astrophysical Journal*, 625, L75
- Hao L., et al., 2005b, *Astrophys. J. Lett.*, 625, L75
- Harrison C., Alexander D., Mullaney J., Swinbank A., 2014, *Monthly Notices of the Royal Astronomical Society*, 441, 3306
- Hawkins M. R. S., Véron P., 1996, *Monthly Notices of the Royal Astronomical Society*, 281, 348

- Heckman T. M., 1980, *Astron. Astrophys.*, **87**, 152
- Hickox R. C., Alexander D. M., 2018, *Annual Review of Astronomy and Astrophysics*, **56**, 625–671
- Hickox R. C., et al., 2009, *Astrophys. J.*, **696**, 891
- Ho L. C., Filippenko A. V., Sargent W. L. W., 1997, *The Astrophysical Journal*, **487**, 568–578
- Horst H., 2008, PhD thesis, University of Kiel, Institute for Theoretical Physics and Astrophysics; University of Heidelberg, Institute for Theoretical Astrophysics
- Hunt, L. K. et al., 2019, *A&A*, **621**, A51
- Ilbert, O. et al., 2006, *A&A*, **457**, 841
- Jaffe W., et al., 2004, *Nature*, **429**, 47
- Jin S., et al., 2023, VizieR Online Data Catalog: “Super-deblended” dust emission in gal. II. COSMOS (Jin+, 2018), VizieR On-line Data Catalog: J/ApJ/864/56. Originally published in: 2018ApJ...864...56J
- Kennicutt R. C., 1998, *Annual Review of Astronomy and Astrophysics*, **36**, 189–231
- Kirkpatrick A., et al., 2012, *Astrophys. J.*, **759**, 139
- Kirkpatrick A., et al., 2013, *The Astrophysical Journal*, **763**, 123
- Kirkpatrick A., Pope A., Sajina A., Roebuck E., Yan L., Armus L., Díaz-Santos T., Stierwalt S., 2015, *The Astrophysical Journal*, **814**, 9
- Kormendy J., Ho L. C., 2013, *Annu. Rev. Astron. Astrophys.*, **51**, 511
- Krolik J. H., Begelman M. C., 1988, *Astrophys. J.*, **329**, 702
- Lacy M., et al., 2004, *Astrophys. J., Suppl. Ser.*, **154**, 166
- Laigle C., et al., 2016, *The Astrophysical Journal Supplement Series*, **224**, 24
- Laloux B., et al., 2022, *Monthly Notices of the Royal Astronomical Society*, **518**, 2546
- Leja J., Johnson B. D., Conroy C., van Dokkum P. G., Byler N., 2017, *The Astrophysical Journal*, **837**, 170
- Madau P., 1995, *Astrophys. J.*, **441**, 18
- Maia M. A., Machado R. S., Willmer C. N., 2003, *The Astronomical Journal*, **126**, 1750
- Malmquist K. G., 1922, *Meddelanden fran Lunds Astronomiska Observatorium Serie I*, **100**, 1
- Mor R., Netzer H., Elitzur M., 2009, *The Astrophysical Journal*, **705**, 298–313

Mouillet A., et al., 2023, arXiv e-prints, p. arXiv:2310.20572

Mullaney J. R., Alexander D. M., Goulding A. D., Hickox R. C., 2011, Monthly Notices of the Royal Astronomical Society, 414, 1082–1110

Nenkova M., Željko Ivezić Elitzur M., 2002, The Astrophysical Journal, 570, L9

Netzer H., 2015, Annu. Rev. Astron. Astrophys., 53, 365

Noll, S. Burgarella, D. Giovannoli, E. Buat, V. Marcillac, D. Muñoz-Mateos, J. C. 2009, A&A, 507, 1793

Pacifci C., et al., 2023, The Astrophysical Journal, 944, 141

Padovani P., Bonzini M., Kellermann K. I., Miller N., Mainieri V., Tozzi P., 2015, Monthly Notices of the Royal Astronomical Society, 452, 1263

Padovani P., et al., 2017, The Astronomy and Astrophysics Review, 25

Pier E. A., Krolik J. H., 1993, Astrophys. J., 418, 673

Polletta M., et al., 2007, Astrophys. J., 663, 81

Prieto A., 2012, Journal of Physics: Conference Series, 372, 012012

Puget J. L., Léger A., 1989, Annual Review of Astronomy and Astrophysics, 27, 161

Rees M. J., 1984, Annu. Rev. Astron. Astrophys., 22, 471

Ricci C., Ueda Y., Koss M. J., Trakhtenbrot B., Bauer F. E., Gandhi P., 2015, Astrophys. J. Lett., 815, L13

Richards G. T., et al., 2006, Astrophys. J., Suppl. Ser., 166, 470

Robotham A. S. G., Bellstedt S., Lagos C. d. P., Thorne J. E., Davies L. J., Driver S. P., Bravo M., 2020, Monthly Notices of the Royal Astronomical Society, 495, 905–931

Sabater, J. et al., 2019, A&A, 622, A17

Salim S., Narayanan D., 2020, Annual Review of Astronomy and Astrophysics, 58, 529

Schmidt M., 1963, Nature, 197, 1040

Scoville N., et al., 2007, The Astrophysical Journal Supplement Series, 172, 1

Seymour N., et al., 2008, Mon. Notices Royal Astron. Soc., 386, 1695

Siebenmorgen, R. Haas, M. Krügel, E. Schulz, B. 2005, A&A, 436, L5

Stalevski M., Fritz J., Baes M., Nakos T., Popović L. Č., 2012, Mon. Notices Royal Astron. Soc., 420, 2756

- Stern D., et al., 2005, *Astrophys. J.*, 631, 163
- Thorne J. E., et al., 2022, *Mon. Notices Royal Astron. Soc.*, 509, 4940
- Tueller J., Mushotzky R. F., Barthelmy S., Cannizzo J. K., Gehrels N., Markwardt C. B., Skinner G. K., Winter L. M., 2008, *The Astrophysical Journal*, 681, 113–127
- Urry C. M., Padovani P., 1995, *Publ. Astron. Soc. Pac.*, 107, 803
- Veilleux S., Osterbrock D. E., 1987, *Astrophys. J., Suppl. Ser.*, 63, 295
- Volonteri M., Haardt F., Madau P., 2003, *Astrophys. J.*, 582, 559
- Wada K., 2015, *The Astrophysical Journal*, 812, 82
- Walcher J., Groves B., Budavári T., Dale D., 2010, *Astrophysics and Space Science*, 331, 1–51
- Weaver J. R., et al., 2022, *The Astrophysical Journal Supplement Series*, 258, 11
- Yun M. S., Reddy N. A., Condon J. J., 2001, *Astrophys. J.*, 554, 803
- da Cunha E., Charlot S., Elbaz D., 2008, *Mon. Notices Royal Astron. Soc.*, 388, 1595
- da Cunha E., et al., 2013, *The Astrophysical Journal*, 766, 13
- da Cunha E., et al., 2015, *Astrophys. J.*, 806, 110

Appendix A

Student Achievement

This is a report of how much research work was done by the student (me) and help done by the supervisor. The data for the research was from the COSMOS 2020 catalogue ([Weaver et al., 2022](#)). The publicly available catalogue was downloaded and matched with the updated photometry catalogue from [Battisti et al. \(2019\)](#) by myself. The combining of the COSMOS2020 ([Weaver et al., 2022](#)) and Super-deblended catalogue ([Jin et al., 2023](#)) was done by my co-supervisor Andrew Battisti.

For SED fitting, the popular MAGPHYS High- z code ([da Cunha et al., 2015](#)) developed by my Supervisor, was installed on the machine by myself. The custom version MAGPHYS + AGN `emp` developed by [Chang et al. \(2017\)](#) was provided to me by my supervisor, and was installed by myself.

The SED fitting for all the galaxies was done and all plots were created by myself. My supervisor suggested adding the torus emission model in the code. The torus emission models were added myself implementing my supervisor's recommendations, including the FORTRAN coding part. In some of the coding parts, my supervisor helped me.

Appendix B

Proposal

B.1 Introduction

B.1.1 Galaxy SED modelling

Galaxies are the building blocks of the universe, which are vast, gravitationally-bound systems consisting of stars, dust, gas and dark matter. Galaxies come in variety of shapes like spirals, ellipticals, lenticulars and irregulars, and the largest of galaxies can span over more than a million light-years across with trillions of stars in it, while the smallest may span over 100s of light-years across with a few thousand stars. We detect galaxies by the radiation emitted across the electromagnetic spectrum from the various process inside a galaxy, the primary source of these being the stellar radiation. The total stellar spectrum of a galaxy is a result of the contribution all the stars in the galaxy. This radiation can be detected by various telescopes which detect the EM radiation across various wavelength of light, for example space based optical telescopes(Hubble Space Telescope, James Webb Space Telescope), or radio telescopes (ALMA- Chile, CSIRO Parkes Telescope- Australia) and so on.

The Spectral Energy Distribution (SED) of a galaxy is a representation of its energy output across the electromagnetic spectrum, providing insights into its physical properties, star formation history, and the presence of components like stars, dust, and gas. A typical SED curve shows energy output as a function of wavelength or frequency, with information on stellar emission, dust emission, gas emission, and active galactic nuclei(AGN). For instance, the peak wavelength or frequency of the SED can be used to determine the temperature of the dominant emission source in the galaxy, while the overall shape of the SED can reveal the age and composition of the stellar populations within the galaxy. Furthermore, AGN activity in a galaxy could be revealed by examining the spectral features, especially in the X-ray or IR part of the spectrum, however it depends on the type of AGN one observes. Similarly, the dust emission features, redshift, emission features, star formation rate, metallicity, gas content of galaxies can be obtained from their SED using various methods. The shape of the SED depends both on the emission from stellar population and the dust in the ISM, because the radiation can be absorbed and reprocessed by dust/gas particles. The radiation in the ultraviolet and

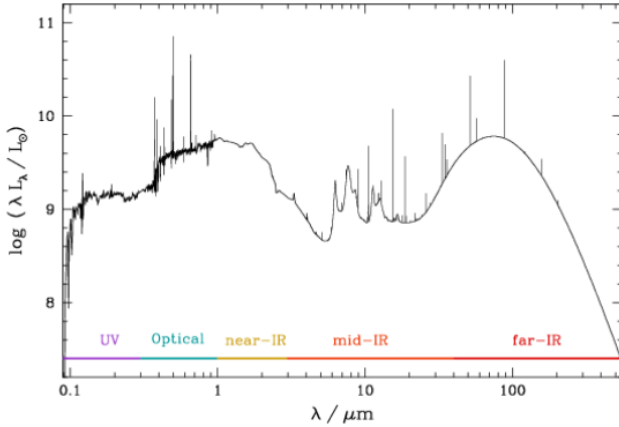


Figure B.1: example SED of a galaxy.(source:da Cunha.2008 ?)

optical wavelength can be absorbed and re-radiated in the longer wavelength (IR range) by the particles. Hence, important information about the dust content of the galaxy can be inferred from the SED of the galaxy. Below shown is the UV to IR SED of a typical galaxy forming $1M_\odot yr^{-1}$.

Galaxy SED models can help us constrain various parameters like star formation rate, specific star formation rate, metallicity, initial mass function, dust luminosity etc, from the observed multi-wavelength emission of the galaxies.

Star formation rate (SFR): Quantifies the rate at which galaxies convert gas and dust into stars (stars are formed by the accretion of dust and gas on to protostars that are formed by the gravitational collapse of dense molecular clouds in the stellar birth clouds of galaxies), typically expressed in solar masses per year. The SFR can be inferred by observing the UV and optical flux of galaxies, which could be by the emission from young stars. The IR emission also accounts for newly formed stars, as it could be the re-emission of the UV and optical spectra from the former, by the dust particles surrounding them.

Specific star formation rate (sSFR): It is a measure of how rapidly new stars are forming in a galaxy relative to its total stellar mass, expressed as the rate of star formation per unit stellar mass and is often used to assess the level of ongoing star formation activity in galaxies, with higher sSFR values indicating more vigorous star formation.

Stellar mass (M_*/M_\odot): The total mass of stars in the galaxy in solar masses.

Metallicity: Abundance of elements heavier than hydrogen and helium in stars and gas of a galaxy, quantifies the proportion of elements like carbon, oxygen, iron, and others. Metallicity is a fundamental property of galaxies and influences their color, spectral features, and evolution. It can provide insights into a galaxy's star formation history, chemical enrichment, and the processes shaping its stellar populations. Galaxies with higher metallicity contain more heavy elements, typically due to greater levels of past star formation and nucleosynthesis.

The Initial Mass Function (IMF): Describes the distribution of stellar masses at the time of their formation within that galaxy. It specifies the relative number of stars in various mass ranges. The IMF characterize the stellar population and analyse processes like star formation, evolution,

and the chemical enrichment of galaxies. The shape of the IMF varies between different types of galaxies and is a key factor in determining a galaxy's star formation rate and luminosity.

Dust luminosity (L_{dust}): Amount of energy emitted by dust particles in a galaxy or a star-forming region, typically in the infrared part of the electromagnetic spectrum. It represents the radiant energy released by the heated dust grains, which have absorbed and re-radiated light from nearby stars. Dust luminosity is an essential component in understanding the overall energy budget and processes associated with star formation and the interstellar medium.

B.1.2 MAGPHYS

MAGPHYS is a model that interpret the mid- and far- infrared SED of galaxies at combined UV, optical and near- IR wavelength spectra, and from this one could derive the physical parameters such as star formation rate, stellar mass, dust content and dust properties of the galaxy. In this model, the Bruzual and Charlot stellar population synthesis code is used to compute the light produced by stars in galaxies, and the angle averaged model of Charlot and Fall(2000) to compute the attenuation of starlight by dust in ISM. The luminosity absorbed and re-emitted by dust in stellar birth-clouds and in the ambient ISM in galaxies is computed and it is distributed in wavelength to compute the infrared SED. Firstly, using Charlot and Fall (2000) model, the luminosity per unit wavelength emerging at a time is a function of star formation rate, luminosity per unit wavelength per unit mass, and effective absorbtion depth of the dust. The total luminosity absorbed and re-radiated by dust is the sum of those contributed by both birth clouds and ISM. While computing the attenuation by dust, the model take into account the fact young stars are attenuated more than older stars due to the dense molecular clouds surrounding them. Also in this model, conservation of energy absorbed and re-emitted by dust, and dust in ISM is heated only by starlight are assumed. Next, the SED by dust in IR is computed by taking account the three main components in the ISM: polycyclic aromatic hydrocarbons(PAHs), very small grains($< 0.01\mu\text{m}$), and big grains(0.01 to $0.25\mu\text{m}$). The PAH emission (strong emission between 3 and $20 \mu\text{m}$) is described by adopting a fixed template. The grey body function used here has the form(Hildebrand 1983):

$$l_{\lambda}^{Td} = \kappa_{\lambda} B_{\lambda}(Td) \left[\int_0^{\infty} \kappa_{\lambda} B_{\lambda}(Td) d\lambda \right]^{-1} \quad (\text{B.1})$$

where $B_{\lambda}(Td)$ is the Planck function of temperature T_d , κ_{λ} is the dust mass absorption coefficient, and l_{λ}^{Td} is normalised to unit total energy. The dust mass absorption coefficient is approximated by: $\kappa_{\lambda} \propto \lambda^{-\beta}$ where β is the dust emissivity index.

The mid IR continuum emission from hot dust(small grains with very small heat capacity and are stochastically heated) is represented as sum of two grey bodies of temperature $T_d = 130$ K and 250 K.

The far IR emission from galaxies is dominated by dust grains in thermal equilibrium with interstellar radiation field at low temperature, two types of these grains considered are warm

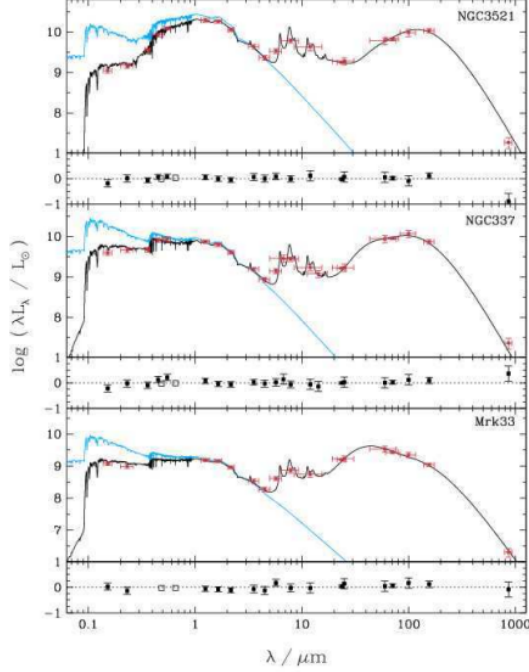


Figure B.2: best model fits (in black) to the observed SED of 3 galaxies (NGC3521, NGC337, Mrk33) using MAGPHYS. source: da Cunha2008 ?

grains(temperature between 30 and 60 K) that reside both in stellar birth clouds and ambient ISM which is represented using a grey body with emissivity index $\beta = 1.5$, and cold grains(temperature between 15 and 25 K) which reside only in ambient ISM, described using greybody spectra with $\beta = 2.0$.

UV, optical and IR SED of galaxies are computed by first computing the total energy absorbed by dust in stellar birth clouds and ambient ISM, and then redistributing it at IR wavelengths. As already mentioned, the adjustable parameters that account for observed relations between various integrated spectral properties are: age, star formation history, stellar metallicity,two components for attenuation by dust and four contributors to IR emission. To constrain these parameters efficiently, a library of combined UV, optical and IR SED of about 661 million models is built, by generating separately a random library of stellar population models, for wide range of star formation histories, metallicities and dust contents, and a random library of IR spectra, for wide ranges of dust temperatures and different dust components that contributes to the total IR luminosity. The best fit parameters are determined from the median likelihood derived by comparing the observed luminosity parameters with the model library and by performing a χ^2 goodness of fit.

MAGPHYS is a successful model that helps in studying the relation between different physical parameters of observed galaxies. The model currently assumes that the only component of luminosity (or, source of energy) in galaxies is from stellar emission. However, some of the galaxies may have a powerful AGN which could provide additional flux to the SED of galaxies, especially in the mid-IR part, which cannot be ignored (Thorne et al.2022 ?). Then it is essential

to separate the AGN component from the SED of a galaxy from the stellar luminosity to obtain the robust physical parameters from SED fitting of galaxies.

B.1.3 Active Galactic Nuclei

Active galactic nuclei(AGN) are compact regions at the centre of a galaxy where a supermassive blackhole(SMBH) accretes matter in the form of gas and dust, to produce immense amount of radiation across the electromagnetic spectrum, which can sometimes outshine the host galaxy (Netzer et al.2015 ?). According to the unified model, an AGN may include several of the components:

- A sub-pc rotational flow accretion disk.
- High density dust- free gas clouds 0.01-.1 pc from the BH (the broad line region, BLR).
- A dusty structure called 'central torus' which has luminosity dependent dimensions of 0.1-10 pc.
- Narrow line region (NLR) that consists of lower density ionized gas that spans from hundreds or thousands of parsecs from the torus.
- Thin molecular maser disk that has size of a torus.
- Central radio jet.

AGNs can be classified into two groups: those having most of the energy output in the form of electromagnetic radiation, resulting from matter accretion through an optically thick accretion disk are "radiative mode AGN", whereas those having primary output transported in two-sided jets are the "jet-mode AGN". The schematic diagram of radiative mode and jet-mode AGN are shown in figure 3. Furthermore, the line of sight (LOS) can affect how we observe and interpret AGNs as well since it affect our angle of view of the central BH, and the obscuration by torus structure.

AGN are classified to various sub-groups, some of which can be discussed here.

Type-I AGNs: They show broad permitted and semi-forbidden emission lines, and are often classified as QSOs or Seyfert 1 galaxies. QSOs are among the most luminous objects in the universe, found in wide range of galaxies and mostly high redshifts, while Seyfert-1 are comparatively less luminous and are found in mostly spiral galaxies and young and local universe. Almost all of the low to intermediate luminosity type-I AGNs show strong, high ionisation narrow emission lines, while narrow emission lines are missing from high-luminosity type-I AGNs. The accretion disk is well developed and luminous for type I AGNs.

Type-II AGNs: They show strong narrow emission lines in the NIR-optical-UV, the strongest lines are $[O\text{ iii}]\lambda 5007$, $[N\text{ ii}]\lambda 6584$, $[O\text{ ii}]\lambda 3727$, $[O\text{ iv}]\lambda 25.9\mu m$, $[Ne\text{ v}]\lambda 3426$, $C\text{ iv}\lambda 1549$ and the hydrogen Balmer and Lyman lines. The dust torus obscures the central nucleus from direct

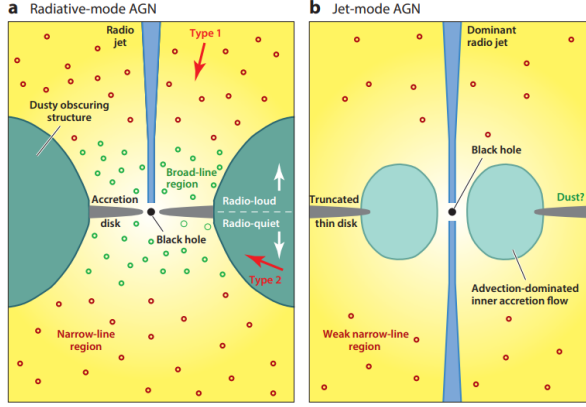


Figure B.3: a) Radiative mode AGN has a geometrically thin, optically thick accretion disk. The dusty torus can sometimes obscure the AGN from some LOS. b) Jet mode AGNs posses a geometrically thick accretion disk, but the dominant source of energy output are the jet. source: Heckman et al. ?

view. They also show a point X-ray source, which is due to the little absorption of X-rays by the torus.

AGNs can also be classified according to how much dust is present in the LOS. The hydrogen column density (N_H) is a measure of the amount of intervening matter between an observer and the object being observed, which is measured as the number of hydrogen atoms (HI) per cm^2 projected along the LOS. Un-obsured AGNs has $N_H \leq 10^{22}$, for obscured AGNs: $10^{22} \leq N_H \leq 10^{24}$, and for Compton-Thick AGNs: $N_H \geq 10^{24}$.

AGN can greatly influence the characteristics of their host galaxies, and by identifying AGN we can better understand how they interact with and affect the larger structure of the galaxy. Moreover, understanding how these black holes have grown and evolved over time is a fundamental question in astrophysics. A considerable fraction of supermassive black holes undergo growth phases that are hidden from direct view due to intervening clouds of dust and gas, which leads to a substantial underestimation of the true population of AGNs in the universe and hence, effective methods to identify AGN population is essential in cosmology.

Identifying AGNs

Some of the methods used for AGN identification can be briefly described here. First, the unobscured AGNs can be observed using the UV-optical photometry. However, the contamination by stellar light and absorption of UV-optical by obscuring dust can limit this observation.

X-ray observation is a powerful method to identify even heavily obscured AGN. The highly energetic X-ray photons at harder rest -frame energies are less affected by the intervening dust and gas, and also the contamination of host galaxy is also low at these rest frames. However, Compton-thick AGNs are X-ray faint because of the heavy obscuration.?

The IR selection is another powerful way of identifying AGN, which accounts to the fact that the UV-optical photons from the accretion disk are absorbed by the dust particles and reprocessed in the mid-infrared and hence heavily obscured AGNs can be identified in IR surveys, as the

obscuring material itself is those emitting this radiation. SED of AGNs in the mid-IR is different than that of normal galaxies. ? Even-though the star formation also creates IR emission by the heating of dust clouds surrounding them, the difference in temperature of medium heated by star formation and AGN activity make the contrast between these two processes, and hence the AGN component in the mid-IR can be separated from the star-formation in the host galaxy. With the SPITZER/IRAC photometry, a large sample of AGNs could be obtained. Various methods like shape of the mid-IR continuum, mid-IR color diagnostics, and template fits to UV-IR photometry were developed to compile AGN samples have been developed basis of the mid-IR selection of AGNs. A limitation of the the broad-band color selection tool is, biased for low-luminosity AGNs if stellar light is bright.

Simultaneous modelling of AGN and host galaxy emission allows for the extraction of AGN luminosity even for low luminous AGN. This requires wide range of wavelength and comparing the observed SED with theoretical templates that represent AGN emission.

B.1.4 MAGPHYS + AGN model

There is a so-far unpublished, modified version of MAGPHYS which contains the contribution by AGN emission to the SEDs, which was used by Chang ? in 2017 for SED fitting of AGNs over the COSMOS field ($0.5 \leq z \leq 2.5$) to derive various galaxy parameters like stellar mass, SFR, dust properties and AGN contribution. In this modified version, the AGN emission is reproduced using a set of empirical AGN emission templates derived from known AGN (see Figure 4). These templates are used to calculate the AGN contribution in the SED of composite galaxies, specifically in the mid- and far- infrared region, and subtract any galaxy contamination. Established intrinsic infrared SEDs for AGNs with can be used to create templates that can be employed to match and analyze the infrared SEDs of composite galaxies, which facilitates the computation of the respective contributions of AGNs and host galaxies to the overall infrared emissions. Template=1 represents low luminosity type-2 Seyfert (Mullaney et al. 2011), template=2 for high luminosity type-2 Seyfert (Mullaney et al. 2011), template=4 for type-1 QSO(Richards et al. 2006; Prieto et al. 2010), template=5 for type-1 Seyfert (Polletta et al. 2007). SED of these templates are shown in figure 4. These four templates are a representative set to ensure global range of AGN known SEDs, and avoid degeneracy in SED fitting. The contribution of the AGN template to the total IR luminosity($\xi_{\text{AGN}} = L_{\text{dust}}^{\text{AGN}} / (L_{\text{dust}}^{\text{AGN}} + L_{\text{dust}}^{\text{SF}})$) is allowed to vary between 0 and 1 for each of the templates. The fitting code is allowed to determine the best fitting template for matching the observations, which involves considering a range of parameters for various AGN contributions and distinct AGN emission templates, ensuring that all possibilities are taken into account.

While Chang et al. compared the IR power-law AGN candidates, the MAGPHYS+AGN fitted consistently and also identified additional AGN. This is shown in figure 5.

Figure 6 shows the SED fitting of QSO with high AGN fraction. The orange line is the SED fitting with AGN component, which is well fitted at MIR compared to the grey line (which is

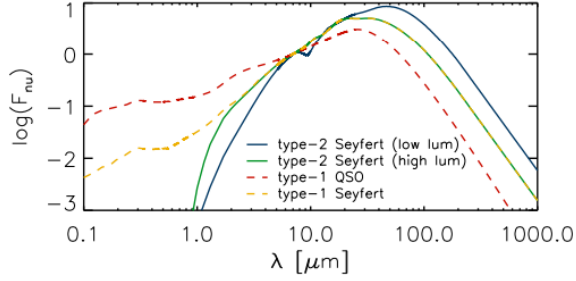


Figure B.4: Four AGN empirical templates used in MAGPHYS+AGN SED fitting. source:Chang et al.2017?

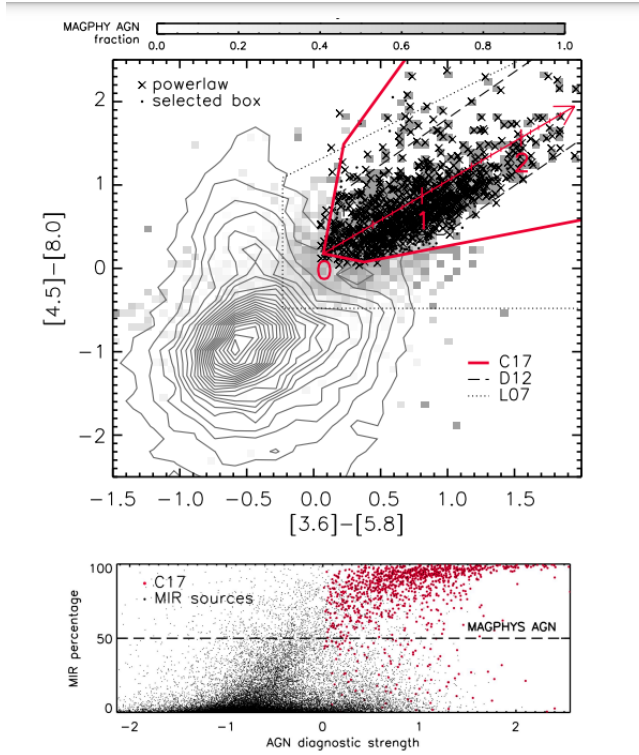


Figure B.5: Upper: IR-AGN selection at $z \leq 2.5$. The cross symbols are galaxies with monotonically rising MIR SEDs. The black dots are IR-selected AGN. contour shows the major population. The gray coding shows the AGN fractions of dominant MIR AGNs according to SED fitting. Lower: The correlation between AGN diagnostic strength and the MIR contribution of AGNs. consistent with power law or MAGPHYS AGNs. source:Chang et al.2017?

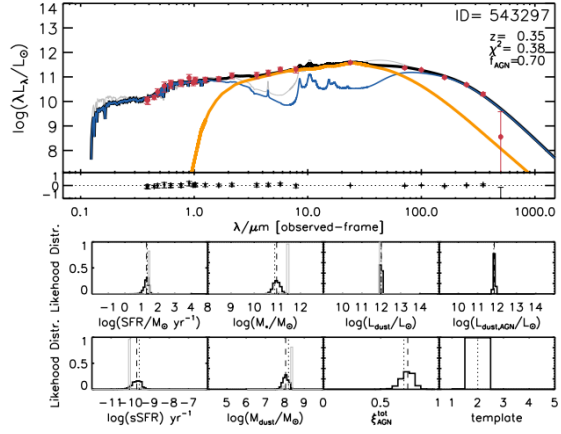


Figure B.6: SED fitting with AGN component (orange line), black line is the best fitting model, blue is the star formation rate. Histogram of the physical parameters are also shown, dash lines are median values and dotted lines are best-fitting values. Here the template=2 is used (high luminosity type-2) source:Chang et al.2017?

the one without AGN component).

The results of Chang et al. included:

- Most of the star formation galaxies contain little AGN contribution.
- AGNs are in higher mass galaxies at all red-shifts.
- MAGPHYS+AGN SED fitting works better than standard fitting by considering MIR contribution.
- Emission of heavily obscured AGNs are dominated by AGN component.
- Many obscured AGNs with high AGN fraction are not detected in the X-ray.

The first part of my project is to test this modified version of MAGPHYS with an AGN component with selected candidates from COSMOS field from the COSMOS2020 catalogue? and investigate if I can reproduce the results of Chang et al.

B.2 Research Plan

The aim of my research is to test the existing MAGPHYS+AGN model for various galaxy candidates, test the efficiency of the model in successfully identifying AGN component, and do necessary modifications to the model if required and investigate additional AGN emission templates from theoretical torus models.

The first step of the project is to run the current version of MAGPHYS+AGN on COSMOS2020 catalogue , which covers a 2 square degree equatorial field with spectroscopy and X-ray to radio imaging by major space-based telescopes and large ground based telescopes, spanning over red-shift range of up to 10.

Next step is to compare the results obtained in this test with other AGN selection techniques like X-ray selection and mid-IR color selection. From this we could analyse how efficient the model is, in identifying known host galaxies with AGN component.

The current version of the model uses 4 empirical templates, as discussed earlier. More torus models can be explored and added to the current version of MAGPHYS and test how the results change according to it. Some of the torus models that are to be explored are the clumpy tori model Nenkova et al.2008?, the flared disc model Fritz et al.2006?, torus model by Siebenmorgen et al.2015?. These models are to be implemented as templates to the MAGPHYS+AGN and SED fitting is to be done for AGN. Check how the results are consistent with other selection techniques. Best-fitting physical parameters are taken into account as well, which includes:

- Star formation rate (SFR)
- specific star formation rate (sSFR)
- stellar mass (M_*/M_\odot)
- dust mass (M_{dust})
- dust luminosity (L_{dust})
- AGN dust luminosity component ($L_{\text{dust,AGN}}$)
- AGN contribution to total IR luminosity (ξ_{AGN})

How the results are affected by the different torus models and templates are to be analysed and update the model using the best results.

We analyse how complex the model needs to be for better identification and parameter-fitting for AGN. The contribution of AGN in the Star formation galaxies, AGN in higher mass galaxies at different redshift, and correlation of obscured AGNs with galaxy parameters are to be analyzed as well. The final part of the project is to apply the new model to new samples of wide redshift range (higher red-shift) including data from JWST and ALMA. The different parameters can be analysed and the correlation between AGN and galaxy physical parameters could be analysed. The whole aim of this project is to develop the SED model that could work simultaneous AGN and galaxy fitting to effectively identify the AGN population in the universe across the cosmic time.

Research Plan

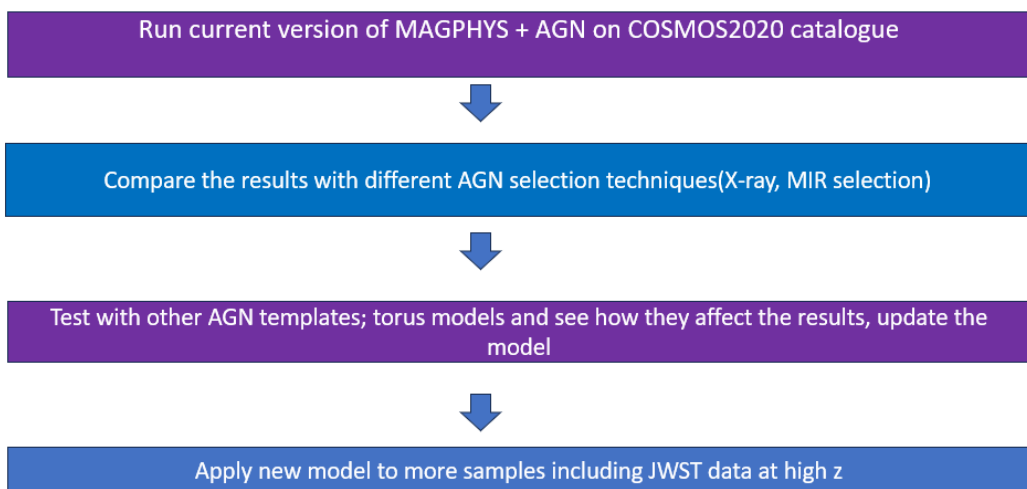


Figure B.7: Summary of research plan

Proposal Bibliography

- Bornancini C. G., Oio G. A., Alonso M., Lambas D. G., 2022, *Astronomy & Astrophysics*, 664, A110
- Chang Y.-Y., et al., 2017, *The Astrophysical Journal Supplement Series*, 233, 19
- Da Cunha E., Charlot S., Elbaz D., 2008, *Monthly Notices of the Royal Astronomical Society*, 388, 1595
- Fritz J., Franceschini A., Hatziminaoglou E., 2006, *Monthly Notices of the Royal Astronomical Society*, 366, 767
- Heckman T. M., Best P. N., 2014, *Annual Review of Astronomy and Astrophysics*, 52, 589
- Laloux B., et al., 2023, *Monthly Notices of the Royal Astronomical Society*, 518, 2546
- Nenkova M., Sirocky M. M., Nikutta R., Ivezić Ž., Elitzur M., 2008, *The Astrophysical Journal*, 685, 160
- Netzer H., 2015, *Annual Review of Astronomy and Astrophysics*, 53, 365
- Siebenmorgen R., Heymann F., Efstathiou A., 2015, *Astronomy & Astrophysics*, 583, A120
- Thorne J. E., et al., 2022, *Monthly Notices of the Royal Astronomical Society*, 509, 4940
- Weaver J. R., et al., 2022, *The Astrophysical Journal Supplement Series*, 258, 11